Nanotomography in the chemical, biological and materials sciences†

Paul A. Midgley,* Edmund P. W. Ward, Ana B. Hungría and John Meurig Thomas*

Received 29th March 2007
First published as an Advance Article on the web 10th May 2007
DOI: 10.1039/b701569k

Nanotomography is a technique of growing importance in the investigation of the shape, size, distribution and elemental composition of a wide variety of materials that are of central interest to investigators in the physical and biological sciences. Nanospatial factors often hold the key to a deeper understanding of the properties of matter at the nanoscale level. With recent advances in tomography, it is possible to achieve experimental resolution in the nanometre range, and to determine with elemental specificity the three-dimensional distribution of materials. This *critical review* deals principally with electron tomography, but it also outlines the power and future potential of transmission X-ray tomography, and alludes to other related techniques.

1. Introduction

Modern medicine has benefited enormously from the practice of three-dimensional imaging involving computed tomography CT (by X-rays or positrons) and magnetic resonance (MR). By contrast, in the chemical sciences only comparatively little advantage has been taken of tomographic techniques, even though it has long been clear that the spatial resolutions ultimately attainable by judicious use of monochromatic X-rays and electron beams far exceed those associated with CT scans and MR imaging of humans.

In nanoscience and nanotechnology it is axiomatic that the size and shape of an object may be even more important determinants of electronic and chemical behaviour than structure and composition.[1] Moreover, nanocrystals, often consisting of one massive cluster,[2] are potentially important materials because their physical and chemical properties may deviate significantly from the bulk crystalline phase. It is generally agreed that the ''nanophase'' length scale where these effects become dominant starts at around 100 nm, and extend downwards to 2 nm or less. A 2 nm diameter nanoparticle of Au or Pd contains some 10^2 atoms, whereas one that has a diameter of 100 nm contains *ca.* 10^8 atoms. Thus, to fix our ideas, we cite some interesting examples: palladium is non-magnetic in the bulk solid state, yet it exhibits non-zero magnetic moments in discrete clusters;[3,4] and gold in its bulk state displays no catalytic activity, yet, as nanoparticles gold is an extremely good catalyst for selective oxidation of hydrocarbons and the complete combustion of carbon monoxide in air.[5–7] The melting point of bulk gold is 1064 °C, while gold nanoparticles of diameter 1.6 nm melt as low as 350 °C.[8] But it is not only size that influences the properties of finely divided solids of colloidal dimension—the shape is also of crucial

---

Department of Materials Science and Metallurgy, University of Cambridge, Pembroke Street, Cambridge, UK CB2 3QZ.
E-mail: pam33@cam.ac.uk; jmt2@cam.ac.uk; Fax: 01223 334567

† Electronic supplementary information (ESI) available: animations corresponding to Fig. 18, 20 and 25. See DOI: 10.1039/b701569k

Paul A. Midgley

Paul A. Midgley is a Reader in Electron Microscopy and Director of the Electron Microscopy Facility at the Department of Materials Science and Metallurgy, University of Cambridge. Before moving to Cambridge in 1997, he held two research fellowships in the H. H. Wills Physics Laboratory at the University of Bristol, the first funded by The Royal Commission for The Exhibition of 1851, the second by The Royal Society. He has studied a wide variety of materials by electron microscopy and developed a number of novel electron microscopy techniques. He has pioneered the use of electron tomography in the physical sciences to visualise three-dimensional morphology, defect structure, composition and electrostatic potential. In 2004 he was awarded the IOM^3 *Rosenhain medal and prize and the FEMS Lectureship. He has written over 100 articles and is invited regularly to speak at conferences around the world.*

Edmund P.W. Ward

Edmund P. W. Ward received BA and MSci degrees in Materials Science from the University of Cambridge, also benefiting from a formative year of study at the Massachusetts Institute of Technology. Since 2004 his research, under the supervision of Paul Midgley, has focused on developing tools for the three dimensional quantification of nanoscale structures. His current interests include the determination of fundamental metrics (such as fractal dimension and surface curvature measures) computed directly using nanotomography.

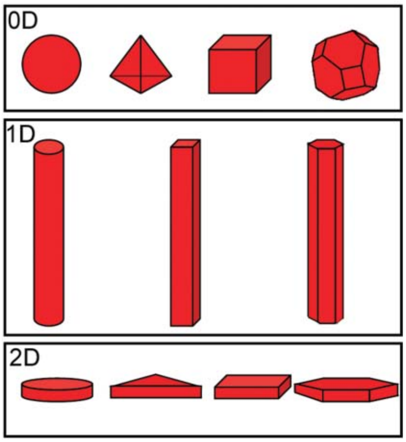

Fig. 1 Basic motifs of inorganic nanocrystals: 0D spheres, cubes, and polyhedrons; 1D rods and wires; 2D discs, prisms, and plates. Reproduced with permission from ref. 8.

importance[8,9] both for elemental materials and also for binary, ternary and more complex structures (such as II–VI semiconductors like CdSe and HgS[9] and abrasive nanomaterials such as ceria).[10] The basic motifs of inorganic nanocrystals (see Fig. 1) range from the zero-dimensional (0D) through to the one and two-dimensional, 1D and 2D, respectively.[8] The need to develop nanotomographic methods applicable to chemical systems (ranging from the physical to the biological) is therefore pressing, just as it is in the engineering and earth sciences.

In this short review we investigate those options that are open to the materials-oriented chemist and, in so doing, after outlining some basic theoretical principles, we present a range of illustrative examples of nanotomographic studies that have greatly enlarged our knowledge of a number of sub-disciplines of the subject, along with contiguous sub-disciplines encompassing parts of biology and medicine. Our focus in this article falls mainly on electron tomography (of which there are several variants), and, in particular on scanning transmission electron tomography which, along with energy-filtered transmission electron tomography, we ourselves have found invaluable in our studies of supported catalysts, nanoalloys and binary II–VI compounds, magnetotactic bacteria and polymers. Whereas the variants of electron tomography are rather fully dealt with and illustrated in this review, we have, for the sake of completeness—and in anticipation of likely future developments—also outlined the rudiments of tomography *via* transmission X-ray microscopy, a technique that will, we believe, find widespread use with greater access to synchrotron X-ray sources.

Retrieving three-dimensional information at the nanoscale involves the application of one (or more) of a number of complementary experimental techniques. Atom probe field-ion microscopy,[11] which is a destructive technique applicable to conducting samples,[12] utilises time-of-flight mass spectrometry for identification of single ions, and combines this with position sensitive detection to produce a sensor capable of determining three-dimensional information with excellent resolution in both location and chemical identity.[13] An alternative, serial sectioning approach, in which a three-dimensional model may be constructed from a series of slices imaged by techniques including atomic force microscopy[14] and cryo-electron microscopy,[15] is in general limited in resolution by the damage introduced in the removal of thin sections. Magnetic resonance imaging (MRI), which extends into the physical sciences with applications including the characterisation of catalytic reactors for laboratory or industrial use,[16,17] has to date been largely restricted to macroscopic systems. Nanotomography *via* MRI is impracticable owing to poor signal to noise ratios. Notwithstanding the vast importance of the aforementioned techniques when applied in their respective fields, in this article we focus on two main techniques that have demonstrable potential in the future deployment of nanotomography to address the issues across the chemical, biological, and materials sciences:

(I) Those based on (soft or hard) transmission X-ray microscopy (TXM) and

---

Ana B. Hungría

Ana B. Hungría was born in Madrid. She obtained her BS degree in Inorganic Chemistry from Complutense University in Madrid. In 2004 she completed a PhD in Physical Chemstry under the supervision of Dr A. Martínez-Arias and Prof. J. C. Conesa working at the "Instituto de Catálisis y Petroleoquímica, CSIC". She is currently doing a postdoctoral stay at the University of Cambridge as a Marie Curie Fellow. Her research interest is the characterization by means of electron tomography of nanoscale structures, mainly heterogeneous catalysts.

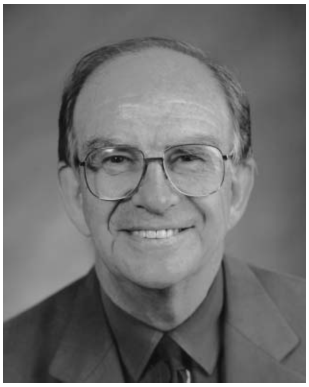

John Meurig Thomas

John Meurig Thomas was one of the first chemists to use and adapt electron microscopy for the study of chemical phenomena, work that he began in Bangor (University of Wales) in the mid-1960s. In his RSC/ACS/Canadian CS organized symposium on Inorganic Chemistry: 'Toward the 21st Century', held in the USA (1982), he highlighted high-resolution electron microscopy and electron energy-loss microscopy as likely major techniques for the materials-oriented chemist of the future. He failed to predict the power of nanotomography (a technique which he started using with Paul Midgley in 1999 to characterize catalysts) or of nanoholography. For his contributions to solid-state chemistry, materials and surface chemistry and especially for his pioneering work in the design and characterisation of solid catalysts he has received numerous awards.

(II) Those based on transmission electron microscopy (TEM).

1.1 Principles

Computed tomography, which involves reconstructing projections of an object viewed from different directions (see Fig. 2), derives from the mathematical principles described by Radon ninety years ago.[18] The *Radon* transform is defined as a mapping into so-called Radon space of a function describing a real space object, by the projection, or line integral, through that function along all possible lines. Thus, given a sufficient number of projections, an inverse Radon transform of this space should reconstruct the object. In practice the sampling will always be limited (see Fig. 3), the inversion will be imperfect, and the goal then becomes to achieve the 'best' reconstruction of the object given the limited experimental data. In addition, a projection of an object at a given angle in real space is a central section through the Fourier transform of that object, the so-called 'central slice theorem'.[19] By recording multiple images (projections) at different angles, many Fourier sections will be sampled, and in principle tomographic reconstruction is possible from an inverse Fourier transform, an approach known as *direct Fourier reconstruction*.[19,20] Although elegant, Fourier reconstruction methods are computationally intensive and difficult to implement for electron tomography, and have been superseded by faster and simpler real space *backprojection* methods.[19,21–24]

The method of backprojection is based on inverting the set of recorded images, projecting each image back into an object space at the angle at which the original image was recorded. Using a sufficient number of backprojections, from different angles, the superposition of all the backprojected 'rays' will reconstruct the original object, see Fig. 2. For more details, see the books by Deans[19] and Herman.[24]

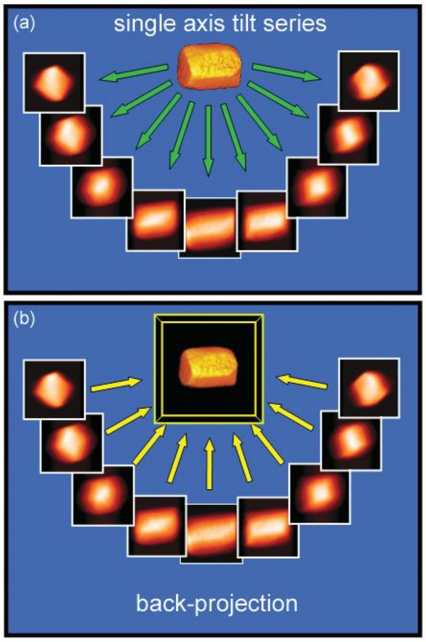

Fig. 2 A schematic diagram of tomographic reconstruction using the back-projection method. In (a) a series of images are recorded at successive tilts. These images are back projected in (b) along their original tilt directions into a three-dimensional object space. The overlap of all of the back-projections will define the reconstructed object.

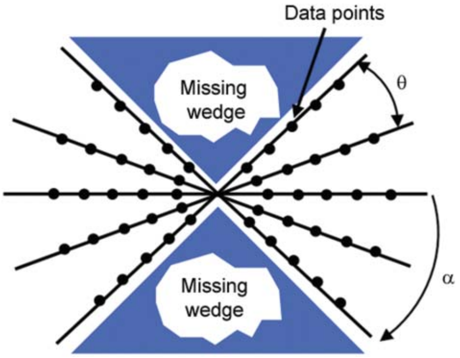

Fig. 3 A schematic plot, shown in Fourier (frequency) space, illustrating the extent of experimental data available after the acquisition of a series of images taken at a range of tilt angles. The angular sampling is θ and the maximum tilt angle is α. Data points lie on slices through Fourier space, which extend radially to higher frequencies from a common intersection corresponding to zero frequency. The relatively small number of data points at higher frequencies can be corrected with the aid of a weighting filter (see text). Also apparent is the missing 'wedge' of information due to the limited range of angles accessible in a typical transmission electron microscope experiment.

Reconstructions using backprojection often appear blurred with fine spatial detail reconstructed poorly, an effect of the uneven sampling of spatial frequencies in the ensemble of original projections. As illustrated in Fig. 3, there is proportionately greater sampling of data near the centre of Fourier space compared with the periphery. It is possible partially to rebalance the frequency distribution in Fourier space by using a weighting filter: a radially linear function in Fourier space, zero at the centre and a maximum at the edge. This improved reconstruction approach is known as *weighted backprojection*.[25] Further enhancements in fidelity may be obtained *via* the use of iterative reconstruction algorithms.[26–31]

1.2 Transmission X-ray microscopy tomography (TXMT)

Although much effort has been involved over several decades in the use of powerful laboratory sources of X-rays (such as rotating anodes) and in the construction of Fresnel zone-plate lenses, where a circular diffraction grating has alternating transparent and opaque concentric rings,[32,33] it is the availability of synchrotron X-ray sources, where high fluxes of controllable monochromatic rays may be readily generated (through the use of dual crystal monochromators), that has greatly transformed the prospects of utilizing TXM for a range of three-dimensional imaging. As in conventional CT practice, X-ray tomography on the nanoscale entails computing (using proven mathematical procedures)[18] from a series of projected two-dimensional (2D) images, taken over as wide a range of angular orientations as possible, the 3D image of the object under investigation. The greater the number of distinct 2D images accumulated, the higher is the resolution of the resulting tomogram (see also Section 2.2.3).

The wide range of X-ray energies that may be selected from synchrotrons enables the powerful addition of chemical sensitivity to 3D imaging. In the soft X-ray region (100 eV to 1 keV) a zone-plate-based TXM[34,35] has achieved a spatial resolution of 15 nm.[36] In the hard X-ray region, because of the difficulty in fabricating the requisite zone-plate lenses, such spatial resolution is not yet attainable, and values of around 60 nm are more typical.[37,38]

The chemical sensitivity of TXM tomography, which comes about because, with synchrotrons, it is readily possible to tune the X-ray energy to be just above or just below a prominent absorption edge of a particular element, is a great advantage especially in the examination of biological materials and hydrated samples. Thus, with soft X-ray TXM, one may operate in such a manner that oxygen (and hence water), where the K-edge energy of the atom is 542 eV, is transparent whereas carbon (K-edge, 284 eV) is opaque if the X-ray energy in the tomography is, say *ca.* 500 eV. Recently,[38] detailed 3D maps of *ca.* 60 nm spatial resolution of several cryogenically fixed, whole, fully-hydrated and unstained biological samples, including individual yeast and bacterium cells have been produced (Fig. 4).[39]

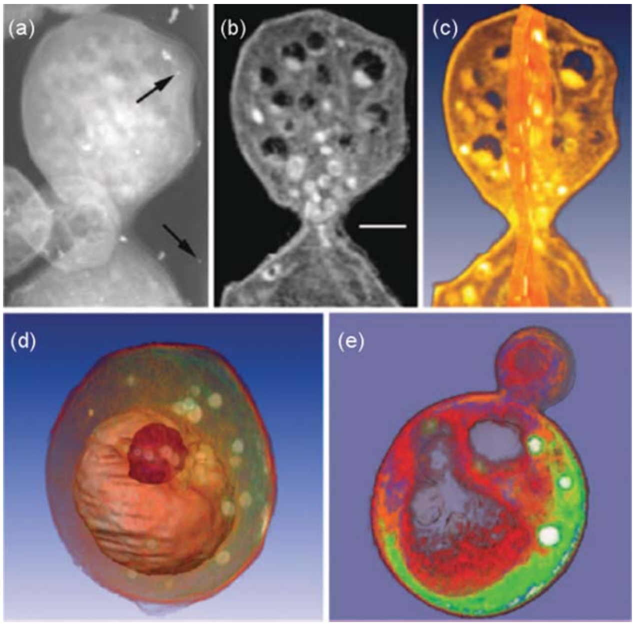

Fig. 4 Tomography of whole yeast cells using TXM. (a) Single projection image of a rapidly frozen budding yeast. The data for the complete three-dimensional reconstruction were composed of 45 such images, collected through a total of 180° of rotation. (b) Computer-generated section through a tomographic reconstruction of the raw data shown in (a). The scale bar is 0.5 μm. (c) Cropped volume rendered view of the reconstructed data from (b). (d) An edge enhancement gradient algorithm was used to volume segment the three-dimensional data used to produce this volume rendered image, showing the nucleus (purple), vacuole (pink) and lipid droplets (white). (e) Color-coded reconstruction of a budding yeast. Lipid droplets, which are the densest structures, were color coded white, the least dense vacuoles were color coded gray, and numerous other subcellular structures or intermediate densities were colored shades of green, orange and red. Reprinted from M. A. Le Gros *et al.*, 'X-ray tomography of whole cells',[39] Copyright (2005), with permission from Elsevier.

In the hard X-ray region (typically 8 to 11 keV) the nanotomographic examination encounters rather more experimental difficulties since the achievable magnification varies with X-ray energy. Benefiting from this range of X-ray energies, however, one may readily access the absorption energies of a wide range of elements that are utilized in the semiconductor industry, *viz.* Cu, Zn, Ga, Ge, As, Ta, W, Au, Hg, Pb, *etc.*[37] Using the the X-ray energy range given above, Yin *et al.*[37] achieved 30 nm spatial resolution in two dimensions; and they obtained impressive 3D images (plus chemical sensitivity) of tungsten plugs such as those used as electrical interconnects between layers in semiconductor integrated circuits (Fig. 5).

In scanning transmission X-ray microscopy, a fine X-ray probe is rastered across the specimen. The resulting image can represent any of a wide range of signals—in addition to density information, it is possible to measure local diffraction, fluorescence, or absorption. Fig. 6 illustrates the chemical sensitivity possible in a tomographic reconstruction based on scanning transmission X-ray microscopy (STXM). Schroer *et al.*[40] combine X-ray absorption near-edge structure (XANES) with scanning microtomography in the hard X-ray range. The sample was scanned in translation through an intensive pencil beam generated at the European Synchrotron Radiation Facility (ESRF) in Grenoble, France. After each full translational scan, during which a full absorption spectrum was recorded at each position, the sample was rotated through 3.6° until 101 projection datasets had been recorded. After filtered backprojection,[41] a full XANES spectrum is available

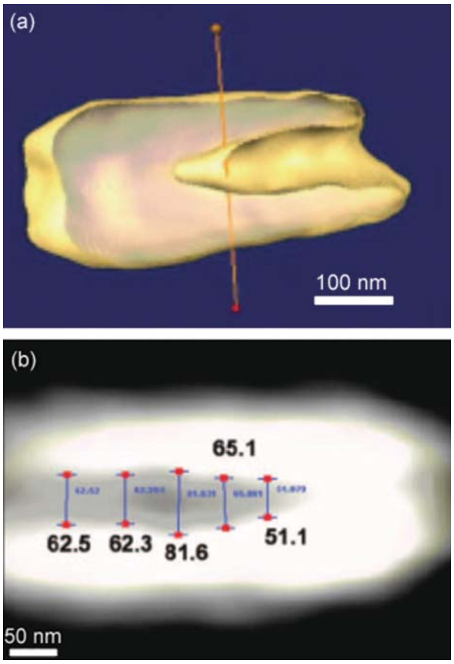

Fig. 5 (a) The side view of a reconstructed tungsten plug displayed using an isosurface, which is a three-dimensional surface contour drawn at equal intensity (brightness) values. (b) The measurement of the size of the keyhole. The diameters of the keyhole range from 50 to 80 nm. Reprinted with permission from G.-C. Yin *et al., Appl. Phys. Lett.*, 2006, **88**, 241115.[37] Copyright (2006) American Institute of Physics.

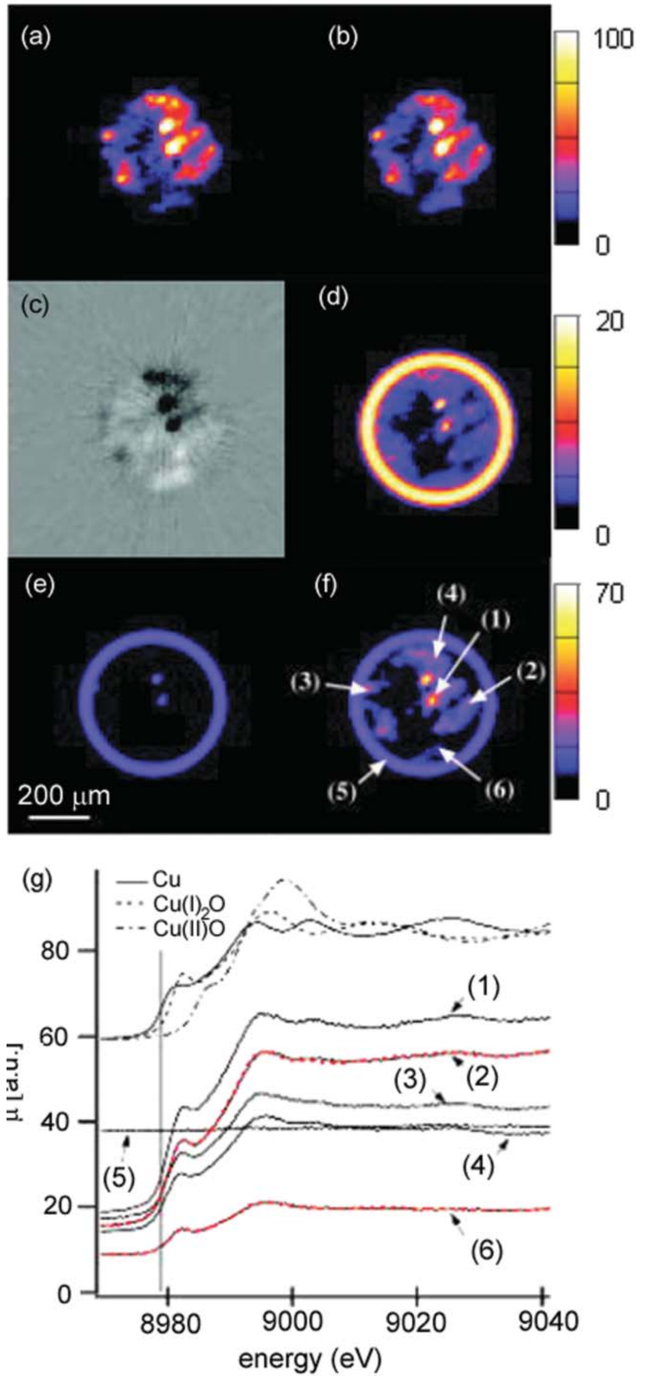

Fig. 6 (a–d): Relative concentrations of (a) metallic and (b) monovalent Cu inside a glass capillary, on the same scale. (c) Difference image between (b) and (a). The shade of gray outside the specimen corresponds to zero difference. Darker areas depict a higher concentration of metallic Cu, while brighter regions signify a higher concentration of Cu(I)$_2$O. (d) Attenuation generated by elements other than Cu. (e–g): Reconstructed tomogram of a capillary filled with a CuO/ZnO catalyst (e) below ($E = 8970$ eV) and (f) above the Cu K edge ($E = 8995$ eV). (g) Reconstructed XANES spectra at different locations marked in (f) and (offset) reference spectra of metallic Cu, Cu(I)$_2$O, and Cu(II)O. The dashed red curves in (g) represent two fits using the reference spectra. Color bars represent the attenuation coefficient, μ, in arbitrary units. Reprinted with permission from C. G. Schroer *et al.*, *Appl. Phys. Lett.*, 2003, **82**, 3360.[40] Copyright (2003) American Institute of Physics.

at each location on any virtual slice through the sample, allowing chemical states to be mapped throughout the sample volume.

Further mechanisms of image contrast remain to be fully exploited in TXM. For example, phase-contrast imaging in addition to (or in place of) absorption may be used.[36] Notwithstanding the difficulties still encountered in zone-plate fabrication, much may be expected from the sophisticated high-resolution X-ray tomographic equipment now being developed at the Advanced Light Source at the Lawrence Berkeley National Laboratory in the USA,[38] and similar facilities (capable of cryo-fixed biotomography) in Japan, Germany[39] and also in Taiwan.[37]

Third generation synchrotrons equipped with undulators open up the feasibility of further advances in X-ray tomography (and in X-ray diffraction microscopy XDM). Because these facilities deliver intense sources of *coherent* electromagnetic radiation they make it possible to achieve coherent X-ray imaging, which uses in-phase X-rays thereby offering a ‘‘lens-less’’ alternative to ordinary X-ray microscopy (that uses Fresnel zone-plates as lenses). This form of X-ray imaging was first suggested by Sayre (in 1980)[42] and first demonstrated at the Brookhaven Synchrotron in 1999, by Miao *et al.*[43]

The procedure in XDM tomography entails three steps:

(I) a tilt series of diffraction patterns are generated using coherent X-rays, providing the amplitudes of the diffracted wave field;

(II) the phases of the wave field are obtained using variants of phase-retrieval algorithms[44] developed in other branches of optics; and

(III) the series of tilt images are recovered by means of Fourier transformation of each individual (fixed angle) data set.

A major development was recently reported by Chapman *et al.*[45] who showed how to accomplish *ab initio* 3D X-ray diffraction microscopy using coherent X-rays. They achieved quite high resolution in all three dimensions: 10 nm in x and y directions and 50 nm in z, and further improvements are expected.

2. Principles of transmission electron microscopy tomography (TEMT)

2.1 Transmission electron microscopy

With monochromatic beams of electrons and electron-optical assemblies that have very low coefficients of spherical aberration,[46,47] the spatial resolution achievable in, for example, scanning transmission electron tomography or conventional TEM, far exceeds that so far attained in TXM tomograpy.

In transmission electron microscopy, an electron beam is projected through a thin sample (typically ~100 nm thick). In conventional TEM, the electron beam is spread to illuminate the whole region of interest. Images are obtained by selecting either directly transmitted or diffracted electrons, to give bright field (BF) or dark field (DF) images, respectively. Scanning TEM (STEM) differs in that a fine focused probe is rastered across the specimen (see Fig. 7). Imaging modes may involve recording the direct beam signal (bright field),

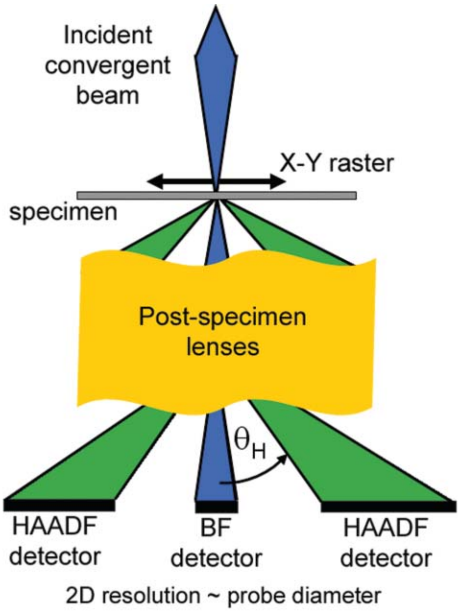

Fig. 7 Schematic diagram of a scanning transmission electron microscope (STEM), showing the position of bright-field (BF) and high-angle annular dark-field (HAADF) detectors. As the probe is scanned across the specimen, the high collection angle (greater than 40 mrad) of the HAADF detector records a signal dominated by incoherent, thermal diffuse scattering. This intensity is insensitive to sample thickness, probe defocus, and the coherent Bragg (diffraction) contrast characteristic of conventional transmission electron microscopy. Reprinted with permission from ref. 48.

diffracted electrons (using an annular dark field detector) or incoherently scattered electrons (with a high angle annular dark field detector).[48] For a detailed presentation of the techniques and results available with TEM, the reader is referred to books by Hirsch *et al.*[49] and Williams and Carter.[50]

2.2 Electron tomography

Although the first experimental demonstrations of electron tomography were made in 1968,[21,51,52] it is only in the past 5–10 years, with the advent of computer-controlled microscopes and increasing image processing power, that electron tomography has become a key technique in the chemical, physical and biological sciences. In the life sciences, there is a pressing need to understand cellular structures, viruses and bacteria; in physico-chemical sciences, there is a need to understand the functional and mechanical behaviour of materials in three dimensions at the nanoscale.[1–4]

2.2.1 The projection requirement. In general, for an image intensity to be usable for tomographic reconstruction it has to be a monotonic function of a projected physical quantity,[53]—the so-called 'projection requirement'. This is often the case in conventional X-ray absorption tomography, as illustrated above, in which image contrast is generated by changes in the X-ray absorption coefficient and sample thickness. In electron microscopy, there are a number of competing contrast mechanisms, only some of which obey the projection requirement. For amorphous materials, such as many biological and polymer structures, contrast in conventional bright-field (BF) TEM images arises from changes in specimen density or thickness and is suitable for tomography.[54] For very weakly scattering specimens, phase contrast images can be used for tomographic reconstructions, rather like the phase contrast images obtained from an X-ray synchrotron source; this method has been used with great success in cryo-tomography in which frozen-hydrated specimens are examined in their 'natural state'.[55] In order to account for the aberrations of the objective lens, and possible contrast reversals of high frequency data, the contrast transfer function (CTF, which measures the deviations from perfection in the diffraction plane due to inevitable imperfections in the objective lens) should be taken into account when interpreting such phase images.[56] For many crystalline materials, dynamical interactions between the electron beam and the crystal potential ensure that, in general, there is no simple relationship between the image intensity and the physical properties of the specimen. Reconstructions, especially from BF images, can show artefacts and poor resolution of internal structure. To combat this, alternative imaging and contrast modes which satisfy the projection requirement have been developed.

2.2.2 Acquisition. As discussed later, the fidelity of a tomographic reconstruction will improve as the number of images used increases. However, the number of images which can be recorded in the electron microscope is limited for two practical reasons. The first is that many samples will be beam-sensitive and thus extended exposure to the beam during the course of the tilt series acquisition will lead to sample damage.[57] The second is that unlike many other tomography methods, electron tomography is undertaken in an instrument with a highly restricted working space and in general it is impossible to tilt beyond a certain maximum angle, either because of the narrow pole-piece gap of the objective lens or because the specimen (if slab-like in morphology) becomes too thick; for example, the projected thickness at 70° tilt is three times that at zero tilt. High specimen thicknesses will lead to a blurred image, through chromatic aberration in TEM, or beam broadening in STEM, and a degradation of contrast, brought about by increasing 'absorption'. [In electron microscopy, 'absorption' normally refers to electrons, scattered to high angles, lost outside the imaging system]. Thus in almost all electron tomography experiments there is a 'missing wedge' of information that is centred about the optic axis, see Fig. 3. To overcome the restricted tilt range, one solution is to prepare a fine 'needle' or 'pillar' specimen and to tilt the specimen about its own axis with an internal tilt mechanism.[58] This allows complete 360° tilt of the specimen without shadowing and without a significant increase in projected thickness.

During acquisition of the tilt series, the image will need to be re-positioned and re-focused after each tilt. Automated acquisition schemes make use of filtered cross-correlation algorithms to determine the shift between successive images. Focus can be corrected in BF TEM by measuring the image shift induced by a small beam tilt.[59] In STEM HAADF imaging, focus is determined by maximising the image contrast.

2.2.3 Reconstruction. The key to high quality tomographic reconstructions is a very well-aligned data set. One of two approaches is normally used: (i) tracking fiducial markers and (ii) cross-correlation. The fiducial technique determines both spatial alignment and the direction of the tilt axis, plus any secondary distortions caused by optical effects.[60] Cross-correlation alignment makes use of the information in the whole image (rather than a few selected points in the fiducial technique) and makes no assumptions about the shape of the support film. It also avoids possible reconstruction problems associated with high contrast objects, such as colloidal gold, which can mask details in the reconstruction. However, cross-correlation alignment does not automatically determine the tilt axis direction and this has to be achieved independently.[61] For dual axis tomography (see later), in which two tilt series are recorded about mutually perpendicular tilt axes, alignment is especially critical. Dual axis iterative reconstruction algorithms also exist and have been shown to be of great benefit for improving reconstruction quality.[62,63]

Assuming that the projections are spread evenly across 180°, the relationship between the number of projections, N, the diameter of the reconstruction volume, D, and the overall resolution, d,[22] has been estimated as:

$$d = \frac{\pi D}{N} \tag{1}$$

However, if there is an upper limit to the tilt angle, this will lead to an anisotropy in the spatial resolution brought about by the 'wedge' of missing information. The resolution is thus degraded in the least-sampled direction, manifesting as an 'elongation' of the object in that direction (usually the optic axis). An estimate of this elongation e, as a function of the maximum tilt angle α,[64] is:

$$e = \sqrt{\frac{\alpha + \sin\alpha\cos\alpha}{\alpha - \sin\alpha\cos\alpha}} \tag{2}$$

For a typical maximum tilt angle of 70°, this leads to an elongation factor of 30%. In the electron microscope, however, samples are often slab-like with far larger dimensions in-plane than in depth and in this case, D should be modified to take this into account:[23]

$$D = t\cos\alpha \tag{3}$$

where t is the (untilted) thickness of the slab and α is the maximum tilt angle. As a consequence, fewer projections are required to attain the same overall resolution.

3. Applications of electron tomography

3.1 Cryoelectron tomography in the biological sciences

In the biological sciences there is a need to bridge the gap between the information attainable at an atomic level by X-ray crystallography and that provided by the dynamic observations of light microscopy (using mainly fluorescence excitation) with a spatial resolution of hundreds of nanometres.[65]

Electron tomography is able to supply three-dimensional information with a resolution of 4–6 nm, once the difficulties with sample preparation and beam damage associated with biological tissues have been overcome. In this regard, to obtain information about the natural 3D distribution of the different components of the entities (cells, organisms and so forth) it is essential both to avoid the collapse of the structures during sample preparation, and to minimize the electron dose during the acquisition of the tilt series.

Alternative methods have been developed for specimen preparation to supersede the traditional dehydration and chemical fixation procedures, which produce aggregation and/or changes in the spatial arrangement of the components. One procedure that has proved to be efficient in keeping the components' intrinsic spatial distribution involves freezing the tissues, either by drastically decreasing the temperature (10,000 K s^{-1}) or by applying a high pressure (*ca* 2,100 bar) during 10–20 ms before cooling in liquid nitrogen.

Marsh *et al.*[66] employed this second method, prior to a freeze substitution to characterise the positional relationships between the different organelles in an insulin secreting cell, achieving a resolution of $\approx$ 6 nm (see Fig. 8). In this study, the reconstruction of part of a cell, including a large portion of the Golgi ribbon, was achieved by acquiring tilt series about two orthogonal axes from each of three serial 400 nm sections, being aligned with one another to produce a total reconstructed volume. Subsequently, a region of ($3.1 \times 3.2 \times 1.2\ \mu m^3$) was analyzed in detail and modelled, allowing the measurement of distances between objects in 3-D and the computation of an average density of neighbouring items as a function of distance between objects. Fig. 8 shows the structural evidence for physical relationships among vesicles, organellar and compartmental membranes in the modelled region.

Cryo-electron tomography emerges as a technique capable of providing 3D information about biological specimens in a frozen-hydrated state, keeping the principal component of the cell, water, in an amorphous state with the rest of the constituents immobilized in a native configuration, and contributing also to increased stability under the beam.[65] Indeed, the presence of water in a vitreous (and not crystalline) state can be used as a hallmark of successful sample preparation and conservation, as well as to test the stability of the specimen during the tilt series acquisition.

This approach has been used to characterize not only whole cells but also different organelles and their components,[67,68] as shown by Baumeister *et al.*[69] for the depiction of nuclear pore complexes (NPC) from *Dictyostelium discoideum*. NPCs are exchange channels that allow the diffusion of ions and small molecules between the cell nucleus and the cytoplasm of interphase cells. After the acquisition of 16 tilt series from frozen hydrated nuclei and the subsequent reconstruction, 267 NPC were extracted and analyzed. Since these NPCs are exchange channels between the cytoplasm and the nucleus, it is possible that they have been immobilized in different transport states. A first analysis was carried out averaging the NPC without prior classification in order to emphasize the common features and characterize the general structure of a *Dictyostelium* NPC, as shown in Fig. 9, where the arrangement and dimensions of the main features are described with a resolution of 8–9 nm. A second, more focused study reveals the existence of two different classes of NPC, a "cytoplasmic

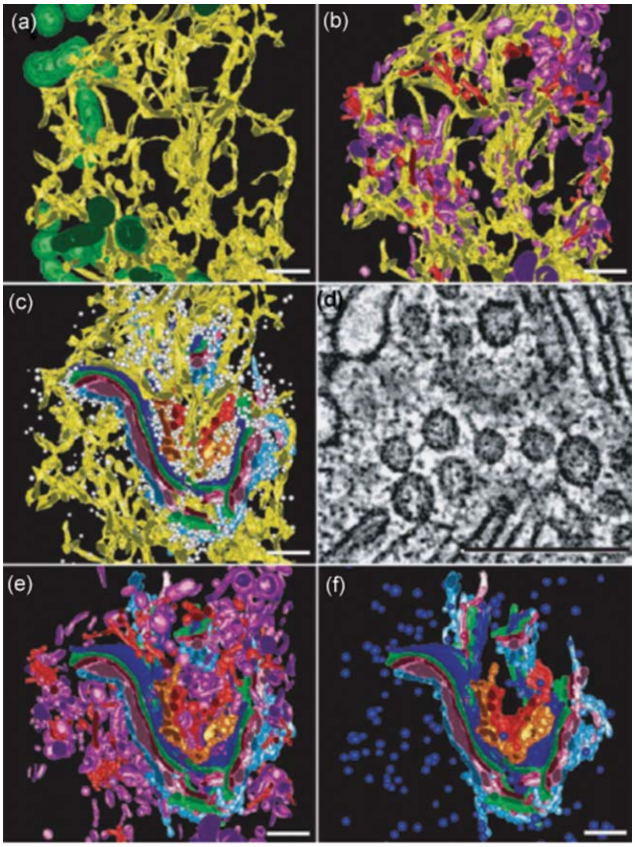

Fig. 8 Structural evidence for physical relationships among different organelles, as determined by Marsh *et al.*[66] using electron tomography and subsequent modelling. The endoplasmic reticulum (ER) is closely apposed to mitochondria (dark green) (a), clathrin-positive (red) and clathrin-negative (purple) endo-lysosomal compartments (b). (c) Here, 2,119 small (average diameter 52 nm), spherical, non clathrin vesicles (white) were distributed close to the Golgi and ER. (d) Higher magnification image extracted from tomographic data showing the numerous tethers connecting small vesicles to each other and to Golgi membranes. Scale bar = 250 nm. (e) Subsets of endo-lysosomal compartments with distinct morphological profiles were clustered together in the Golgi region. (f) Here, 132 dense core vesicles (bright blue; average diameter 100 nm) were present in the Golgi region but were apart from the Golgi stack. Scale bars = 500 nm (except (d)). Reprinted from B. J. Marsh *et al.*, *Proc. Natl. Acad. Sci. U. S. A.*, 2001, **98**, 2399–2406.[66] Copyright (2001) National Academy of Sciences, USA

filament class" (CF) and a "luminal spoke ring class", according to the size, shape and position of the central plug/transporter (CP/T) located within the central channel.

Another interesting application of cryoelectron tomography is the characterization of the magnetosome chains of magnetotactic bacteria, together with the identification of the molecular factors controlling its organization.[70,71] These magnetosome chains contain 15–20 magnetite crystals of *ca.* 50 nm which because of their superparamagnetism orient the bacteria, such that they swim parallel to the earth's magnetic field. 3D reconstruction of individual cells were obtained by means of dual-axis tilt cryoelectron tomography, showing that each magnetite crystal was surrounded by a layer that was an invagination of the cell membrane, along with the presence of some filaments parallel to the chain.

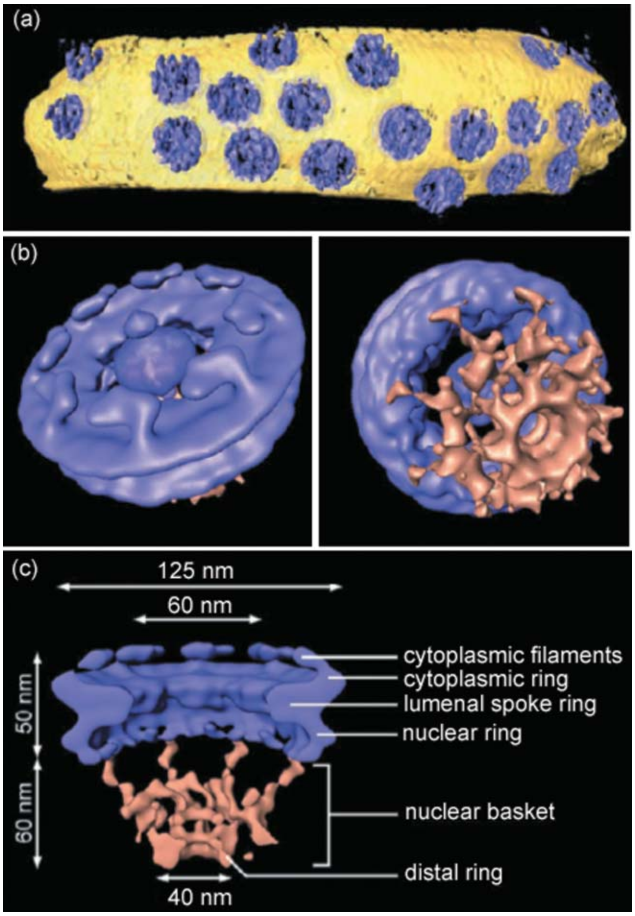

Fig. 9 Electron tomography has revealed the structure of macromolecular cellular assemblies, such as the nuclear pore complexes (NPC) from *Dictyostelium discoideum* depicted here. (a) Surface-rendered representation of a segment of nuclear envelope (NPCs in blue, membrane in yellow). The dimensions of the rendered volume are 1680 nm × 984 nm × 558 nm. The density of NPCs was $\sim$45 mm^{-2}. (b–c) The structure of *Dictyostelium* NPC. (b) (left panel) Cytoplasmic face of the NPC. The cytoplasmic filaments are arranged around the central channel; they are kinked and point toward the central plug/transporter (CP/T). (right panel) Nuclear face of the NPC. The distal ring of the basket is connected to the nuclear ring by the nuclear filaments. (c) Cutaway view of the NPC with the CP/T removed. The dimensions of the main features are indicated. All views are surface-rendered (nuclear basket in brown). From M. Beck, *et al. Science*, 2004, **19**, 1387–1390.[69] Reprinted with permission of AAAS.

Fig. 10 shows the cryo tomography study performed after the identification of the gene Mamk, which is thought to have an essential role in the formation of functional magnetosomes (for more details see ref. 71). The 3D reconstruction of a wild cell (Fig. 10(a)) can be compared with the visualization of a MamK-deficient mutant cell (Fig. 10(b)), in which instead of long aligned chains of magnetic crystals, only small clusters are observed. The alignment of the magnetic crystal and the formation of the filaments can be reversed by means of the mutant cells being complemented with Mamk-GFP (green fluorescence protein –GFP– fusioned to the C terminus of MamK), as shown in Fig. 10(c).

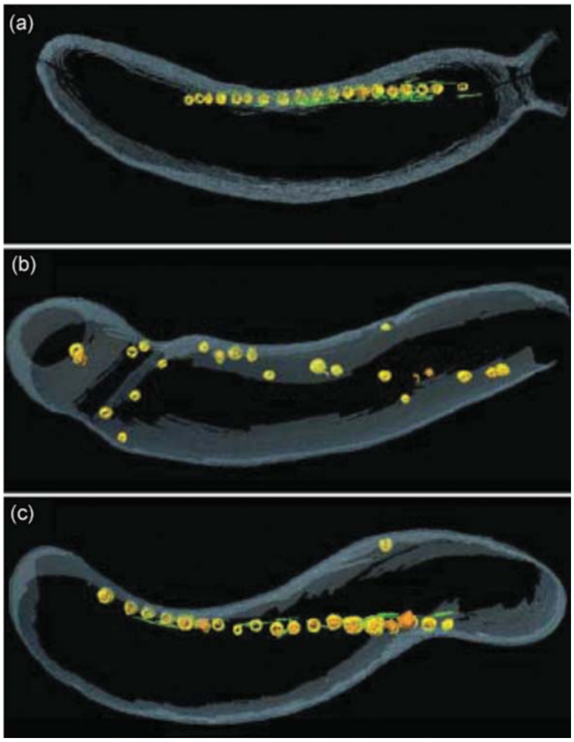

Fig. 10 The MamK gene is required for the proper organization of the magnetosome chain in magnetotactic bacteria, as illustrated by this tomographic study. (a) Three dimensional reconstruction of a wild-type AMB-1 cell. The cell membrane (gray), magnetosome membrane (yellow), magnetite (orange), and magnetosome-associated filaments (green) are rendered. (b) ΔmamK mutant, where magnetosomes appear disordered and no filaments are found in their vicinity, (c) ΔmamK cell expressing mamK-GFP on a plasmid showing full reversal of the mutant phenotype. From A. Komeili *et al.*, *Science*, 2006, **311**, 242–245.[71] Reprinted with permission of AAAS.

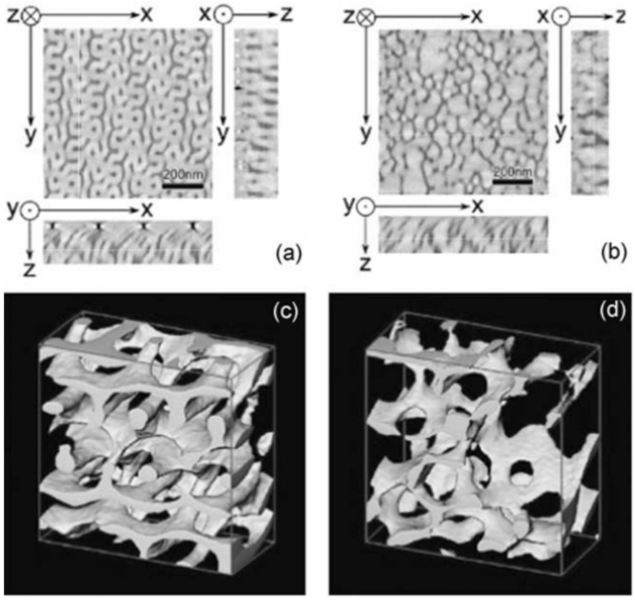

Fig. 11 Two dimensional planar and cross-sectional slices of (a) ordered and (b) disordered bi-continuous morphologies seen in block copolymers generated from BF TEM tomographic reconstructions. (c) and (d) are corresponding 3D solid renders of microdomains within an electron-transparent polymer matrix. For details of the system, see text. Reprinted with permission from ref. 73.

3.2 TEM and STEM tomography in the physical sciences

One of the earliest examples of the use of electron tomography in the physical sciences[54] was in the characterization of complex morphologies found in block copolymers.[72] A similar but more recent study by Jinnai *et al.*[73] using bright-field TEM examined the bicontinuous morphology that results by adding a relatively high molecular weight homopolymer (polystyrene homopolymer, S) to a microphase ordered (poly (styrene-block-isoprene), SI) diblock polymer. Fig. 11 shows the tomographic reconstruction of the two coexisting bicontinuous morphologies, one ordered (resembling the gyroid motif with *Ia*3*d* symmetry), and one disordered. The reconstructed data shown in Fig. 11 are used to provide quantitative analysis of the composition of the morphologies and to provide real space insights into their structural characteristics, such as mean curvature (H) and Gaussian curvature (K), parameters which define the local shape of any curved surface.

In the physical sciences in particular, the number of image modes that have been adapted for electron tomography has increased in recent years. As well as conventional BF tomography, as practised predominantly in the life sciences, more unconventional modes have been used such as so-called weak-beam dark-field[74] tomography to form 3D reconstructions of dislocation networks[75,76] and holographic tomography used for 3D reconstructions of electrostatic potentials.[77] However, perhaps the two most useful modes for nanotomography, particularly across the physical and chemical sciences are HAADF STEM tomography and energy-filtered transmission electron microscopy (EFTEM) tomography.

3.2.1 HAADF STEM imaging. The predominantly coherent nature of low-angle scattered electrons means that conventional BF and DF images are prone to contrast reversals from changes in specimen thickness, orientation or defocus. But high angle scattering is predominantly incoherent, and STEM images formed using a scanned focused probe together with a high-angle annular dark field (HAADF) detector (see Fig. 7), do not suffer the contrast changes associated with coherent scattering.[78]

In simple terms, high angle scattering is brought about by the interaction of the electron beam with the atom nucleus. As such the cross-section for HAADF scattering can be approximated to that given by Rutherford scattering and in the unscreened limit it is proportional to the square of the atomic number, Z^2. This sensitivity to composition together with the incoherence of the scattering process enables small heavy particles to be made highly visible within a matrix or support (see Fig. 12).[48,79] In practice the exact dependence, particularly for crystalline specimens, is a function of many other factors, which need to be determined before any quantification can take place.[80] One key factor is the inner angle of the HAADF detector, θ_{HAADF}, which must be large enough to ensure coherent effects are minimal. As a guide $\theta_{\mathrm{HAADF}} \geqslant \lambda/d_{\mathrm{thermal}}$ where λ is the electron wavelength and d_{thermal} is the amplitude

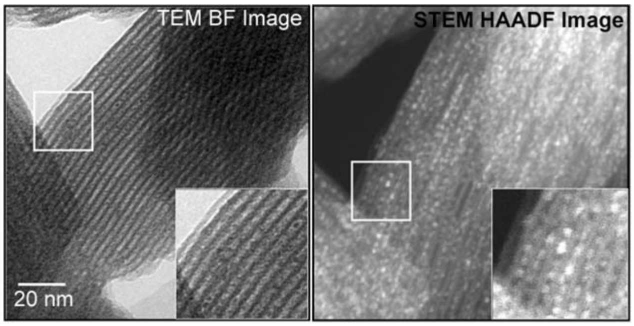

Fig. 12 A comparison of transmission electron microscope images obtained using TEM BF (left) and STEM HAADF (right) on identical areas of a catalyst. Nanoparticles of [$Ru_{10}Pt_2$], invisible in BF, are clearly seen in the HAADF image. Reprinted with permission from ref. 48.

of atomic thermal vibration.[81] For Si at 200 kV, $\theta_{\mathrm{HAADF}} >$ 40 mrad.

Although STEM HAADF imaging is essentially incoherent in nature the intensity of the image can be modified by the orientation of a crystalline specimen. Near a major zone axis, strong Bloch wave channelling tends to concentrate the beam intensity onto the atomic columns as it propagates through the crystal.[82] This increases the relative current density at atomic cores, increasing the high-angle scattering and consequently the intensity in the HAADF image.[83] However, it will be significant only at a small number of orientations and thus in a small number of images within the series. Therefore, the effect of channelling-enhanced contrast tends to have limited effect on the tomographic reconstruction. Thus, to a good approximation, the intensity of STEM HAADF images varies monotonically both with atomic number and specimen thickness, thus satisfying the projection requirement.[84,85]

If the specimen is slab-like and tilted to high angles, only part of the specimen will be in focus. By rotating the scan, the tilt axis of the specimen can be made perpendicular to the direction of the rapid STEM scan. Given the geometric relationship between tilt, specimen height and defocus it is possible, for every scan line, to adjust the beam focus to account for the change in specimen height. A focal ramp can then be applied across the image to minimise problems associated with the limited depth of field, a method known as 'dynamic focusing'. One should note that for very thick or massive specimens, with large average scattering angles, a significant proportion of scattering may fall outside the outer edge of the detector and lead to contrast reversals, and strong deviation from monotonic behaviour.[86]

3.2.2 Electron tomography in the study of solid catalysts. Another early application of TEM tomography was the study of solid catalysts by de Jong *et al.*[87–90] These investigations used bright-field TEM to elucidate the nature of the porosity of zeolites and nanoporous silica and the distribution of finely divided noble-metal catalysts within them. A striking example of the efficacy of this work is shown in Fig. 13, where internal mesopores within an acid-leached specimen of the acidic forms of mordenite (a good hydro-treating catalyst) and zeolite Y (the catalyst of choice for cracking of hydrocarbons) are seen.

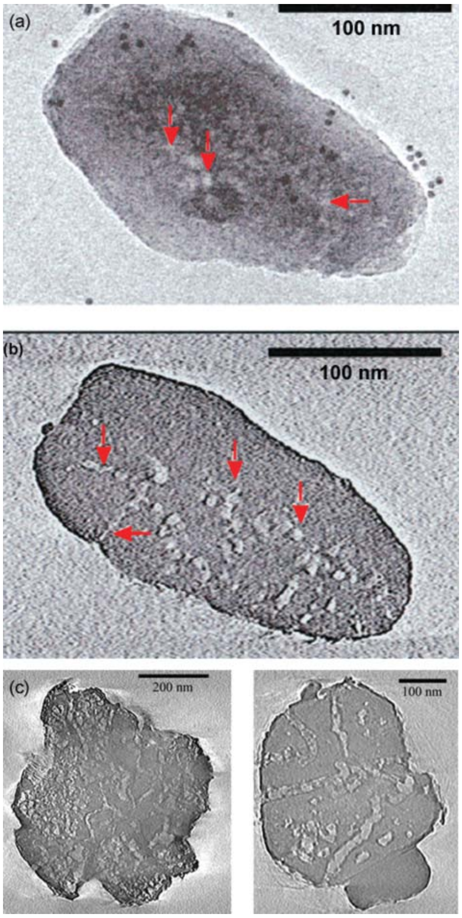

Fig. 13 (a–b) Mesopores in an intact acid-leached H-mordenite crystal. (a) Conventional TEM image indicating the mesopores in the crystallite (white spots, arrows) and several gold beads (black dots, 5 nm in diameter) on the grid for the alignment. (b) Digital slice (0.6 nm thick) through the 3D reconstruction of the crystallite showing the mesopores inside the crystallite (arrows). Reprinted with permission from ref. 88. Copyright (2000) American Chemical Society. (c) Digital slices through bright field electron tomographs of hydrothermally treated zeolite Y, showing extensive internal pores. Reprinted with permission from ref. 87. Copyright (2002) American Chemical Society.

What is vividly revealed in the tomographic slices shown in these figures are the "sealed" internal pores within the solid catalyst. These are inaccesible to gas molecules and so the gas-absorption method of determining porosity[91] and pore-size distribution is shown to be unrealiable by this tomographic study. In adition to probing the internal meso- and micropores of zeolitic and other nanoporous solid catalysts TEM nanotomography is ideally suited to the study of the distribution, size and composition of supported nanoparticle catalysts, such as the bimetallic ones investigated in this laboratory.[92–95] In these bimetallic systems ruthenium is frequently one of the principal constituents, *e.g.* Ru_5Pt, $Ru_{10}Pt_2$, $Ru_{12}Cu_4$ and Ru_6Sn. For the visualization by TEM tomography of the minute nanoparticles such as $Ru_{10}Pt_2$ (diameter *ca.* 1 nm), we have shown[48] that it is better to use HAADF rather than bright-field (BF) imaging. As noted above, the atomic number sensitivity of HAADF imaging results in excellent contrast when viewing (heavy) metal

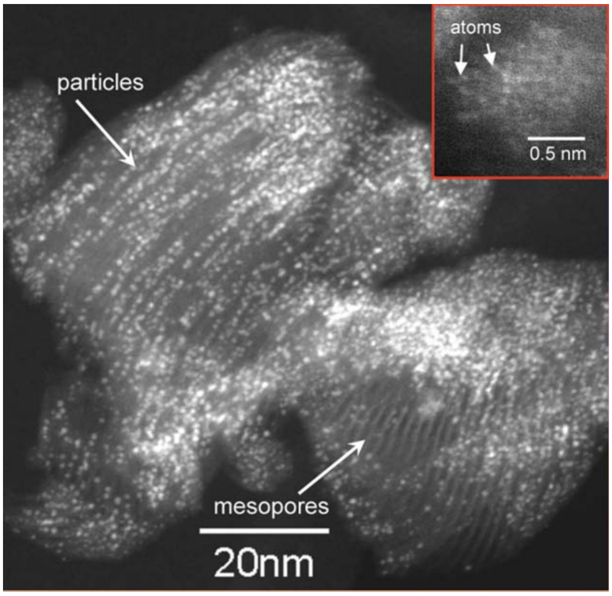

Fig. 14 STEM HAADF image of $Ru_{10}Pt_2$ supported on mesoporous silica of the ordered, MCM-41 type (note alignment of clusters along the pores). The inset shows one of the particles at high magnification. For more details see ref. 96.

particles supported on or within a (light) matrix. Nanoparticles anchored along the interior surface of nanopores within mesoporous silica are invisible in BF but readily visible in HAADF images (Fig. 12 and 14).[96] Tomographic reconstructions of mesoporous silica-supported $Ru_{10}Pt_2$ bimetallic catalysts are shown in Fig. 15. The position of individual nanoparticles within a single mesopore may be readily discerned in this tomographic study (Fig. 15 (d)).

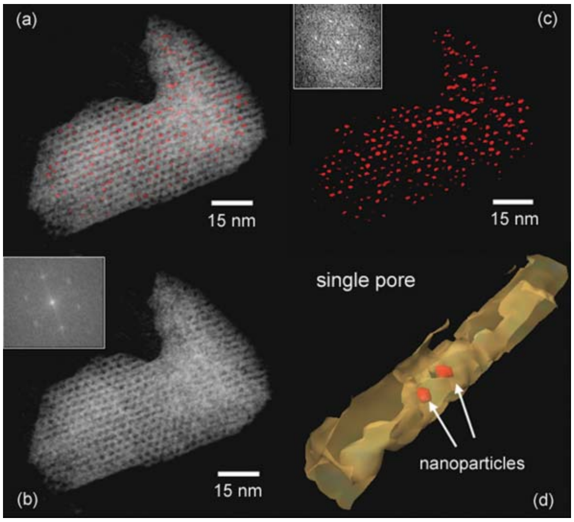

Fig. 15 (a) Voxel projection of a tomographic reconstruction of a heterogeneous catalyst composed of Pt/Ru nanoparticles (red) within an MCM-41 mesoporous silica (white). The two components are separated in (b) and (c); their insets are power spectra (computed diffractograms) revealing the hexagonal symmetry. (d) The position of two nanoparticles within a single mesopore. Reprinted with permission of Blackwell Publishing from P. A. Midgley *et al.* 'Nanoscale scanning transmission electron tomography'.[103]

Apart from the three-dimensional character of the tomographic images shown here, two extra advantages of HAADF STEM tomography are seen to good effect. First, with the high spatial resolution attainable in modern aberration-corrected STEM instruments, individual atoms supported on the mesoporous silica may be clearly imaged (see arrows in inset of Fig. 14). Second, the precise composition of an individual particle may be determined by X-ray emission spectroscopy,[94] as illustrated in Fig. 16. This extra facility has proved particularly useful in our recent study of trimetallic nanoparticle selective hydrogenation catalyst supported on silica[97] (see Fig. 17). The highly localized probe that constitutes the electron beam (diameter *ca.* 1 nm) is far superior to delocalized beams of X-rays that would be used to determine composition—in a spatially averaged fashion—by, say X-ray fluorescence spectroscopy.

Nanoparticle metallic or bi- and tri-metallic catalysts are currently of great interest, not only because of their high performance in a variety of selective hydrogenations,[92,98,99] but also because of their structural and electronic properties.[100] It

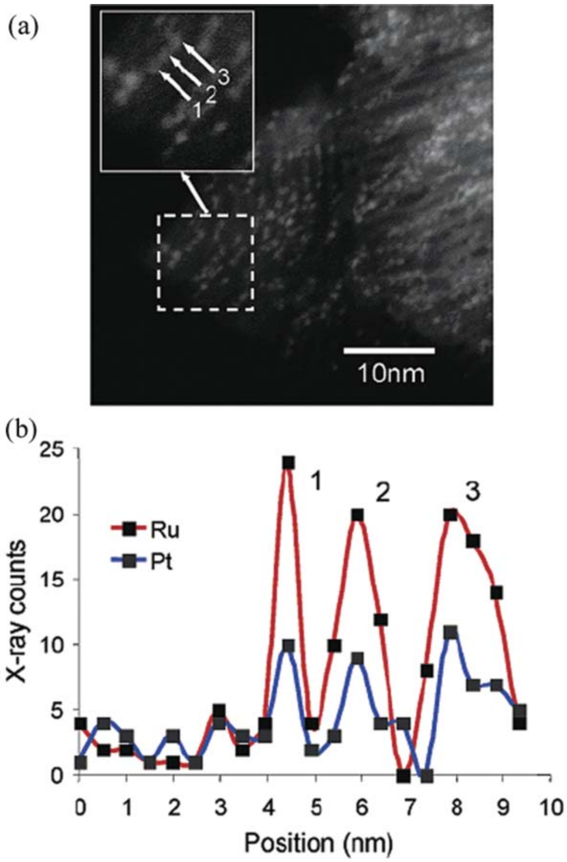

Fig. 16 (a) STEM HAADF image of the Ru–Pt-based catalyst. The inset shows the particles studied by X-ray microanalysis. X-ray spectra were recorded approximately every 0.5 nm and the resulting compositional profile across the 3 particles is shown in (b). From the area under the curve in the region of the three nanoparticles, the ratio of Ru : Pt for each particle is determined as 5 : 1, in line with the composition expected from stripping the carbonyl groups from the precursor $[Ru_{10}Pt_2(CO)_{28}]^{2-}$ dianions. Reprinted with permission from ref. 94. Copyright (2004) American Chemical Society.

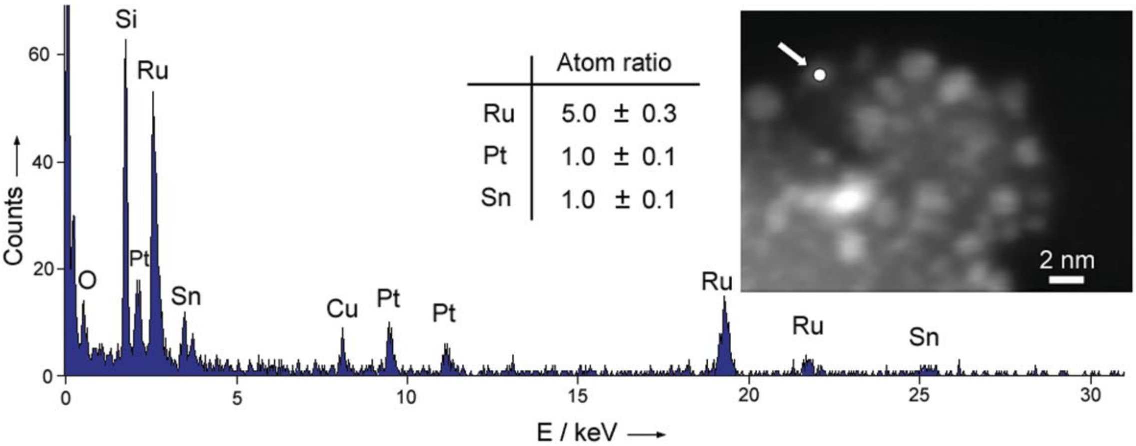

	Atom ratio
Ru	5.0 ± 0.3
Pt	1.0 ± 0.1
Sn	1.0 ± 0.1

Fig. 17 Electron-induced X-ray emission spectrum of nanoparticles of Ru_5PtSn nanoclusters on a mesoporous silica. The arrow in the inset points to the particle for which this emission spectrum was recorded. The peak for Cu in this spectrum originates from the sample holder and grid. The tabulation refers to the results of 8 different X-ray emission spectra. Reprinted with permission from ref. 97.

is desirable to develop tomographic techniques that have atomic resolution. So far the only tool capable of this degree of spatial discrimination is the destructive one of field-ion tomography (FIT). Several series of molecular dynamics runs performed on Au–Pd nanoparticles by Yacamán *et al.*[101] simulate the melting transition of the bimetallic system. FIT could, in principle, track the changes in local structure and composition of the kind of bimetallic nanoparticles described by Yacamán *et al.* in the context of pre-melting phenomena.

3.2.3 STEM tomography for structure determination. Embedded carbon nanotubes[102] have generated considerable research interest across many disciplines, and electron tomography remains the best technique for investigating the morphology of heavy metals embedded within the tubes. In Fig. 18, encapsulated magnetic iron particles, used as a growth catalyst, can be clearly identified within the multiwall nanotubes.[103] The three-dimensional information allows the investigation of the relationship between tube morphology and particle location. In addition, it illustrates that high-fidelity reconstructions are possible using STEM HAADF images even from specimens of low atomic number such as carbon. Furthermore, the sample may be studied using a range of complementary electron microscopy techniques, such as electron holography[104]—the inset shows a phase reconstruction from an electron hologram revealing the stray magnetic field lines associated with one of these iron particles.

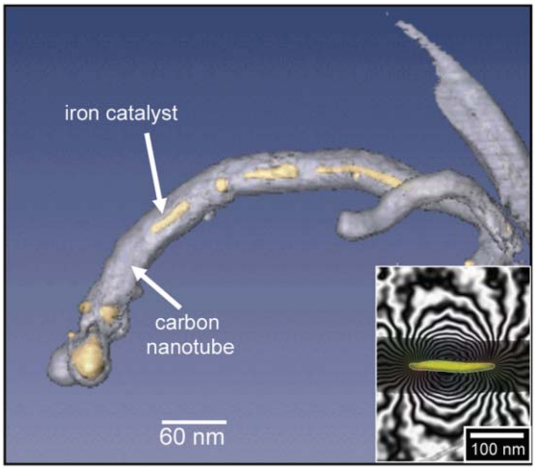

Fig. 18 A surface-rendered reconstruction of a multiwall nanotube in which a number of magnetic iron particles have been encapsulated.† The ferromagnetic state of the iron is demonstrated by the holographic phase image of the inset. Reprinted with permission of Blackwell Publishing from P. A. Midgley *et al.* 'Nanoscale scanning transmission electron tomography'.[103]

Fig. 19 illustrates the ability of STEM HAADF tomography to reveal the internal architecture of nanostructures, and highlights the excellent contrast available when imaging regions of differing atomic number.[117] Furthermore this reconstruction, which derives from a series of images recorded every 2° from −76° to +76°, has captured the internal morphology with sufficient resolution to index the crystal faces. The results are obtained from a single magnetotactic bacterial cell of strain MV-1 that contains a chain of 60 × 35 nm magnetite (Fe_3O_4) crystals. Such bacteria have been of interest in part because similar crystals were found in Martian meteorite ALH84001.[105] Fig. 19(a) shows a voxel projection of the tomographic reconstruction revealing the three-dimensional structure of the magnetite chain and an outline of the outer bacterial membrane. Reconstructed slices taken from the end (labelled 1) and the centre (labelled 2) of a single crystallite are shown in Fig. 19(b), and the superimposed regular hexagon (dotted) emphasises the perfection of the magnetite crystal. The ability to reconstruct the 3D internal architecture of nanoscale structures offers the possibility of using electron tomography for 3D nanoscale metrology. Such metrology is likely to be of great importance for the verification and calibration of nanoscale devices and structures in the future.

As mentioned earlier ordered mesoporous silicas are excellent supports for a range of nanoparticle bimetallic catalysts of high activity and selectivity in the hydrogenation of a range of key organic molecules.[106] The cubic variant MCM-48 (a = 23 nm) of the MCM (Mobil catalytic material) series of silicas has a complex gyroid-like three-dimensional

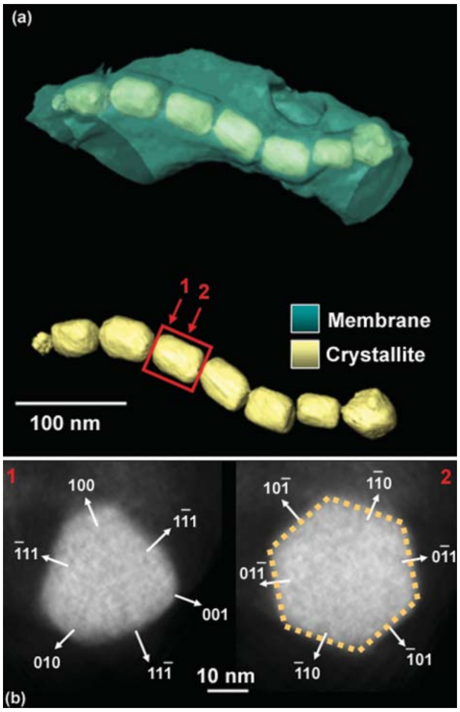

Fig. 19 (a) A tomographic reconstruction of magnetotactic bacteria strain MV-1. (b) Digital slices from the boxed crystal in (a). The reconstruction of the 'backbone' reveals the perfect crystal faceting of the cubic crystals, as revealed by the superposition of a regular hexagon (yellow dashes) on slice 2. Reprinted from M. Weyland *et al.* 'Nanoscale analysis of three-dimensional structures by electron tomography',[117] Copyright (2006) with permission from Elsevier.

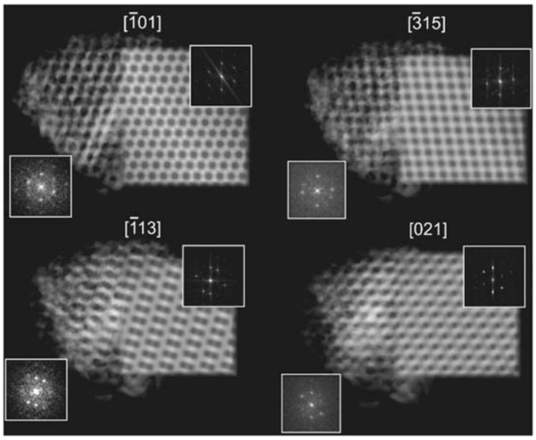

Fig. 20 A montage of tomographic voxel projections of MCM-48 shown as successive major zones axes as the three-dimensional tomographic reconstruction is rotated about a <112> zone axis. For full details see text.† Reprinted from T. J. V. Yates *et al.* 'Three-dimensional real-space crystallography of MCM-48 mesoporous silica revealed by scanning transmission electron tomography',[108] Copyright (2006), with permission from Elsevier.

pore network, as determined by analysis of the structure factors derived from electron diffraction experiments.[107] The cubic phase, MCM-48 is intrinsically superior to its hexagonal analogue MCM-41 in that pores run in three mutually perpendicular directions in the former whereas they run in only one direction in the latter.

The significant advantage of studying this system with electron tomography was the ability to visualise the pore-structure directly. As well as providing a model-independent structure solution, tomography, being a direct imaging technique, further provided the opportunity to reveal any deviations from the perfect crystal structure, such as twin boundaries.[108] A series of 158 STEM HAADF images was acquired every 1° between −78° and +79°. Fig. 20 shows a montage of voxel projections computed from a three-dimensional tomographic reconstruction of a sub-100 nm particle of MCM-48 silica.[108] Each projection is at a major zone axis encountered when rotating about a <1 1 2> axis through a symmetry-independent sector of reciprocal space. A {1 1 2} plane, whose normal is vertical in the plane of the paper, is common to all projections. On the right of each image is a simulation of the MCM-48 structure based on an approximate gyroid surface. Power spectra (computed diffractograms) for both experiment and simulation are shown as insets. The agreement between experiment and simulation is remarkably consistent for each projection. Based on the direct 3D information available from electron tomography, the structural model was revised to better match the observed pore size and distribution. The original model was based on studies[107] in which the complementary pore sizes of MCM-48 were determined based primarily on pore volumes modelled from nitrogen gas adsorption–desorption experiments; in the future, direct structural measurements available with STEM tomography should overcome some of the limitations of such model-dependent analyses.

A concluding example of high-resolution structure determination is given in Fig. 21, which demonstrates the improvements in fidelity that can be realised when a tomographic reconstruction is based on a dual axis series.[62] A single-axis reconstruction of CdTe tetrapods reveals some legs have not been reconstructed, due to the effects of the missing wedge. By taking two perpendicular tilt series and reconstructing their combination, the structure of the tetrapods is fully revealed.

3.3 EFTEM tomography

Energy-filtered transmission electron microscopy (EFTEM) is based on acquiring two or three, or sometimes a large series, of energy-filtered images near an ionisation edge of interest. Compositional information from an energy loss image may be isolated by generating either a background-subtracted elemental map (from three or more images) or a jump-ratio map (a division of a post-edge image by a pre-edge image). Accounting for inelastic cross-sections, both maps will show intensity that is related to the amount of an atomic species and, to a reasonable approximation, EFTEM maps fulfil the projection requirement for tomographic reconstruction.[109,110] A schematic of the EFTEM technique is shown in Fig. 22 for a post-column imaging filter; in-column filters, for example the 'omega' filter, positioned between the objective lens and the projector lens system, are also used for EFTEM.[111]

For elemental maps, the conventional three-window approach takes little account of diffraction contrast, which

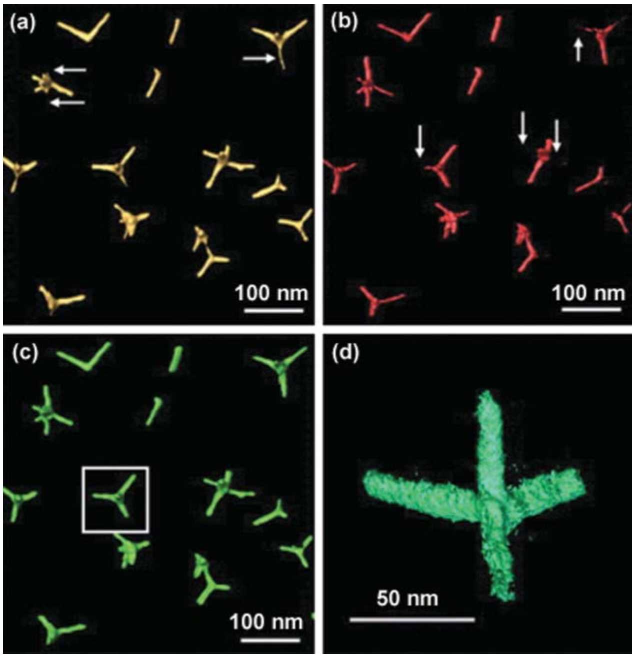

Fig. 21 3-D reconstruction of a dual axis tilt series. (a) is a reconstruction of the first tilt series and shows that some of the legs of the CdTe tetrapods are missing or weak, due to the missing wedge, as indicated by the arrows. (b) is a reconstruction of the perpendicular tilt series showing that while the missing legs in (a) are present in this data set, there is now a different set of missing legs, again indicated by the arrows. (c) is a dual axis reconstruction of the two data sets and illustrates that all legs are well reconstructed—because the missing information has been minimized. The tilt axes in (a) and (b) are parallel to the direction of the arrows. (d) Detailed view of the tetrapod selected in (c). Reprinted from I. Arslan *et al.* 'Reducing the missing wedge: High-resolution dual-axis tomography of inorganic materials',[62] Copyright (2006), with permission from Elsevier.

may affect the validity of the projection assumption, as it would for a BF image. Such contrast can be minimised by dividing the elemental map by the zero-loss image, but this can introduce further artefacts due to changes in image resolution as a function of energy loss.[112] Jump-ratio images can be used to remove diffraction contrast in the energy loss images but image intensity values are not quantitative. The jump ratio increases with thickness, in an approximately linear fashion up to a value comparable to the overall inelastic mean free path, λ. Beyond this thickness, the jump-ratio decreases primarily because the energy loss background intensity rises faster than the ionisation edge signal. Therefore, thicker areas may give rise to anomalously lower jump-ratio values, which invalidates the projection requirement. In practice, rapidly changing diffraction contrast in EFTEM maps tends to be averaged out over the tilt series and results primarily in an increase in reconstruction background intensity.

By acquiring an extended series of images over the energy loss edges of interest, fully quantitative elemental maps can be generated.[113,114] Tomographic reconstructions from a tilt series of energy loss images generates a large four-dimensional dataset (x, y, z, ΔE), from which a great deal of 3D structural and spectral information can be gleaned.[115]

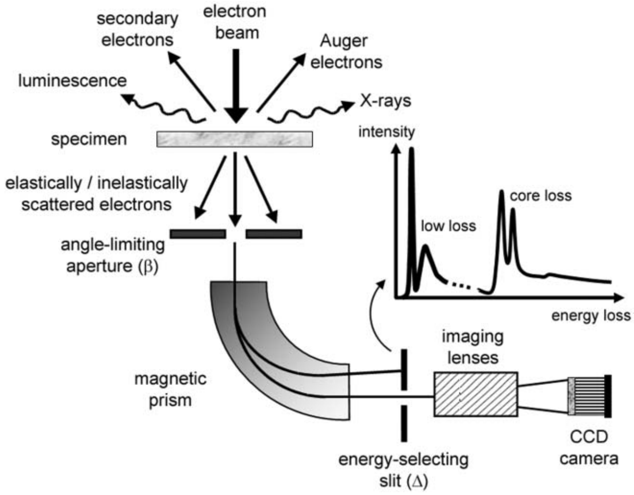

Fig. 22 A schematic diagram illustrating the acquisition procedure for energy-filtered TEM (EFTEM). Beam-specimen interactions generate a characteristic spread in the energy of transmitted electrons which can be dispersed using a magnetic prism. At a line focus of the prism, electrons of a given energy may be selected using an energy-selecting slit and a further series of lenses used to generate an image on a CCD camera using only those electrons allowed to pass through the slit. Image courtesy of P. J. Thomas and M. Weyland.

The resolution of EFTEM is controlled by a number of factors: delocalisation, chromatic aberration, spherical aberration and the diffraction limit.[57] In most cases the dominant term is the chromatic aberration of the objective lens. This leads to a blurring of the filtered image which can be minimised by reducing the slit width or the collection angle (typically the objective aperture) but always at the expense of total signal. One of the main factors that limits extensive use of EFTEM tomography is the effects of dose on beam-sensitive samples,[57] but despite this limitation, initial studies have successfully applied EFTEM tomography to map phosphorus-containing ribosomes within a cell,[116] see Fig. 23.

A simple but highly illustrative example of EFTEM tomography in the physical sciences is shown in Fig. 24. Here an EFTEM tilt series has been acquired from a chain of nanospheres composed of an iron-nickel alloy which has been oxidised.[117] One issue that was addressed was whether the spheres had sintered together and then the whole ensemble oxidised or whether the spheres had oxidised and then agglomerated into the chain. A tilt series was acquired and at each tilt a large energy loss series was acquired that spanned the energy range from the zero loss to beyond the nickel edge. Fig. 24 (a) shows a BF zero loss image together with an iron, nickel and oxygen elemental map reconstructed at zero degree tilt. The elemental information has been colour coded in the single EFTEM map in (b). From this single projection, it appears that the oxide shell is present between the spheres.

Fig. 24 (c) shows a central slice through the 3D reconstructed oxygen map where it is evident that the metal spheres had sintered together first and then the whole chain oxidised afterwards. This simple example highlights the power of this form of 3D compositional tomography.

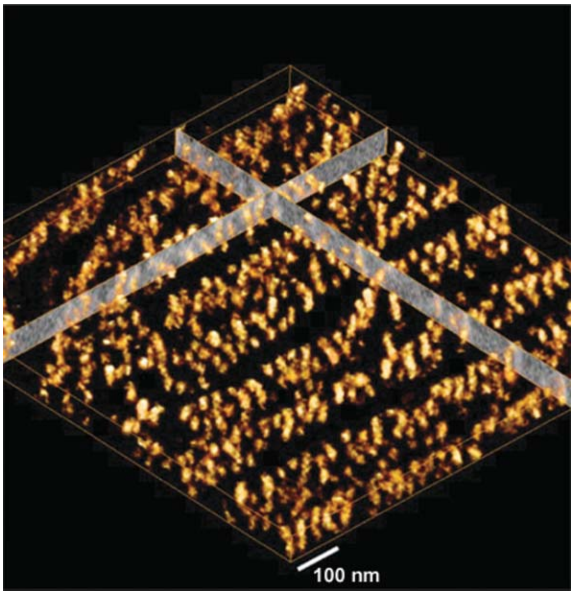

Fig. 23 Volume-rendered, tomographic reconstruction of phosphorus in a section of nematode, *Caenorhabditis elegans* cell. Rows of ribosomes are evident along stacks of endoplasmic reticulum membranes. Slices through the reconstruction in the *x–z* and *y–z* planes are also shown. Reprinted from R. D. Leapman *et al.* 'Three-dimensional distributions of elements in biological samples by energy-filtered electron tomography'.[116] Copyright (2004), with permission from Elsevier.

By combining an energy loss series with a tomographic tilt series a large four-dimensional dataset (x, y, z, ΔE) can be acquired.[113,114] An example of this is shown in Fig. 25 in which a low loss EFTEM series has been recorded from a composite structure composed of multi-wall carbon nanotubes (MWCNT) and nylon. Optimal image contrast was found by dividing low loss images separated by about 6 eV, corresponding closely to the maxima in the plasmon resonance for the nanotubes and the nylon, see Fig. 25 (a) and (b). However, by using the whole energy loss series, it is possible to reconstruct a series of energy loss tomograms and then extract spectral information from sub-volumes of the reconstructions. This process is known as volume-spectroscopy,[115] and a schematic is shown in Fig. 25 (c–e). Low loss volume-spectra extracted from different sub-volumes of the nanotube-nylon composite are shown in Fig. 25 (f). Finally it is possible to examine the 3D structural information as seen in the surface rendered views of Fig. 25 (g–h).

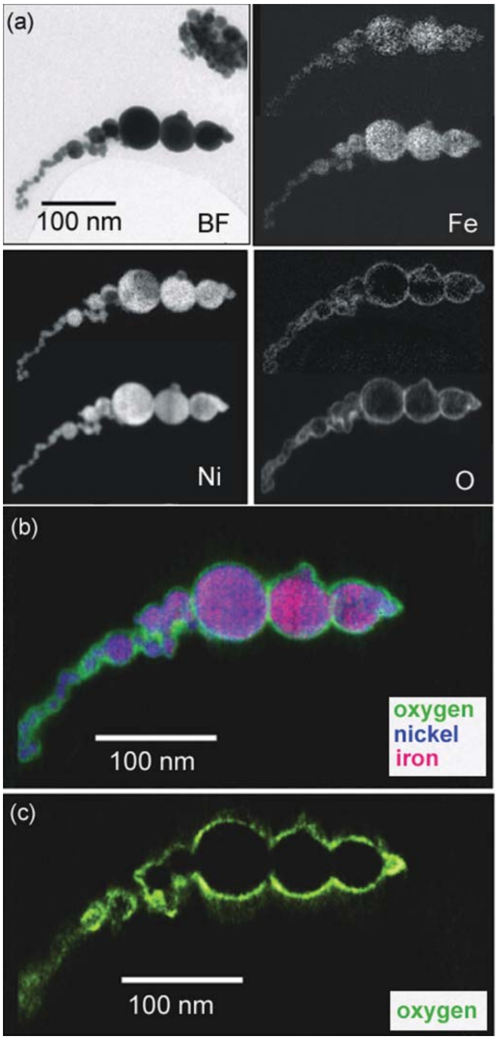

Fig. 24 (a) Zero loss bright-field image and two-dimensional elemental maps of nickel, iron and oxygen recorded from a chain of FeNi nanoparticles chosen for EFTEM tomography acquisition. The lower elemental maps are generated by re-projecting the tomographic reconstructions in the zero tilt direction. The upper elemental maps are the equivalent raw conventional elemental maps. (b) RGB voxel (volume pixel) projection of the combined reconstructions of the FeNi nanoparticles. (c) A slice through the oxygen tomographic reconstruction proving how the oxide covers the ensemble of nanoparticles rather than individual nanoparticles. Reprinted from M. Weyland *et al.* 'Nanoscale analysis of three-dimensional structures by electron tomography'.[117] Copyright (2006) with permission from Elsevier.

Conclusions and outlook

The need to understand physico-chemical functions at the nanoscale is common across many scientific disciplines. Such understanding will only be fully realised if techniques are available that allow full 3D characterisation with high spatial resolution and high fidelity. In this review we have given a number of examples of nanotomography across the chemical, biological and materials sciences. High quality tomograms can now be acquired almost routinely that demonstrate subtle and important variations in structure and composition with nanometre resolution. In the near future, it should be possible to reconstruct tomograms of 3D physical properties, such as strain, electrostatic potentials and magnetic fields, and indeed the first proof-of-principle examples of this are now published.[75,77] In addition, the coupling of *in-situ* and environmental microscopy with tomographic reconstructions[118] will certainly prove to be a powerful combination and should allow deeper insights into, for example, the growth of nanotubes and nanorods and enable a better understanding of the chemistry of catalysts at the nanoscale.[119]

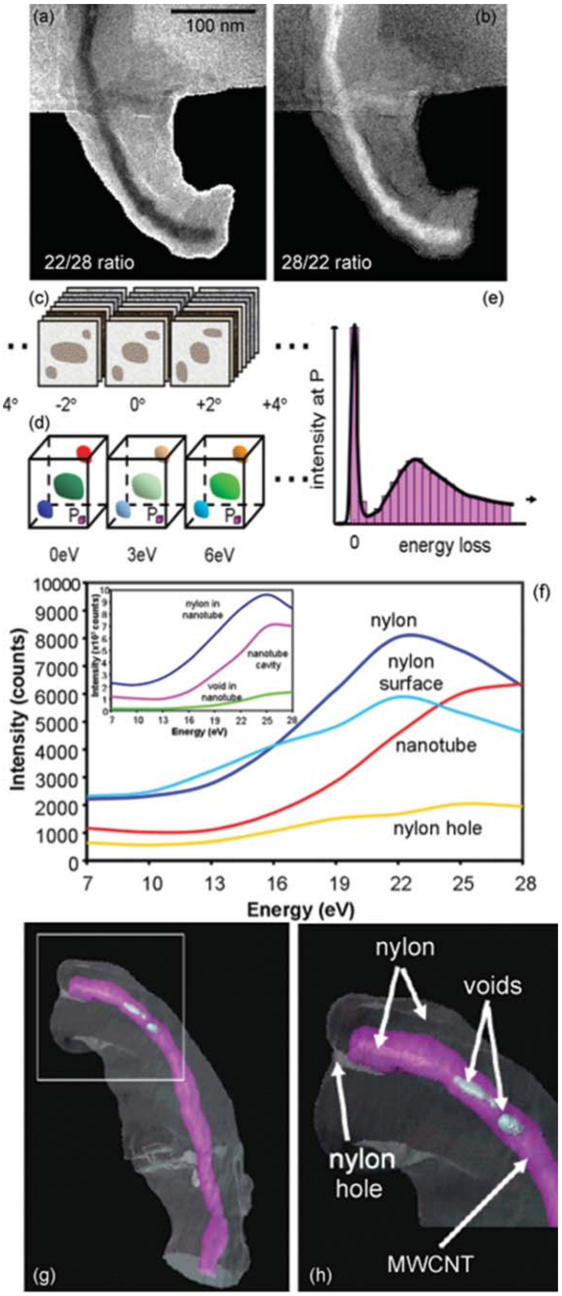

Fig. 25 Energy-filtered tomographic analysis of a composite structure composed of multi-wall carbon nanotubes (MWCNT) and nylon.† (a,b) Images formed from the ratios of the two plasmon energy loss images 22 eV/28 eV and 28 eV/22 eV respectively. (c) A schematic demonstrating the collection of an energy-loss series at each tilt. (d) The tomographic reconstruction at each energy window showing a specific voxel P in the 3D volume. (e) The reconstructed energy-loss spectrum obtained by extracting the intensity of the voxel P from each reconstructed energy-loss window. (f) Low loss spectra have been reconstructed by extracting the intensity from the same voxel in every reconstructed energy-filtered tomogram. Spectra from the bulk nylon, the MWCNT, the nylon surface, and a hole in the nylon are shown in the main figure, while spectra extracted from the nanotube cavity are shown in the inset. (g,h) Surface render of the nanotube (purple) and nylon (grey) from the tomographic reconstruction of the plasmon ratio 28 eV/22 eV. Reprinted with permission from ref. 115. Copyright (2006) American Chemical Society.

Acknowledgements

The authors thank Ilke Arslan, Jonathan Barnard, Rafal Dunin-Borkowski, Mhairi Gass, Lydia Laffont, Joanne Sharp, Jenna Tong, Matthew Weyland and Timothy Yates for their tomographic contributions. PAM thanks the EPSRC, FEI company and the Isaac Newton Trust for funding. ABH thanks the European Community for a Marie Curie Research Fellowship. EPWW thanks the EPSRC and Fitzwilliam College, Cambridge for financial support.

References

1 E. Roduner, *Chem. Soc. Rev.*, 2006, **35**, 583–592.
2 R. L. Johnston, *Dalton Trans.*, 2003, **22**, 4193–4207.
3 B. V. Reddy, S. N. Khanna and B. I. Dunlap, *Phys. Rev. Lett.*, 1993, **70**, 3323–3326.
4 M. Moseler, H. Häkkinen, R. N. Barnett and U. Landman, *Phys. Rev. Lett.*, 2001, **86**, 2545–2548.
5 A. Haruta, *Chem. Rec.*, 2003, **3**, 75–87.
6 M. S. Chen and D. W. Goodman, *Acc. Chem. Res.*, 2006, **39**, 739–746.
7 A. S. K. Hashmi and G. J. Hutchings, *Angew. Chem., Int. Ed.*, 2006, **45**, 7896–7936.
8 Y. W. Jun, J. S. Choi and J. Cheon, *Angew. Chem., Int. Ed.*, 2006, **45**, 3414–3439.
9 M. A. El-Sayed, *Acc. Chem. Res.*, 2004, **37**, 326–333.
10 X. D. Feng, D. C. Sayle, Z. L. Wang, M. S. Paras, B. Santora, A. C. Sutorik, T. X. T. Sayle, Y. Yang, Y. Ding, X. D. Wang and Y. S. Her, *Science*, 2006, **312**, 1504–1508.
11 M. K. Miller, A. Cerezo, M. G. Hetherington and G. D. W. Smith, *Atom Probe Field Ion Microscopy*, Oxford University Press, Oxford, 1996.
12 Recent developments in the atom probe technique, notably the introduction of pulsed lasers, extend the scope of atom probe tomography to the investigation of some semi-conducting and non-conducting samples.
13 M. Peet, S. S. Babu, M. K. Miller and H. K. D. K. Bhadeshia, *Scr. Mater.*, 2004, **50**, 1277–1281.
14 Y. Chen, J. Y. Cai, T. Zhao, C. X. Wang, S. Dong, S. Q. Luo and Z. W. Chen, *Ultramicroscopy*, 2005, **103**(3), 173–182.
15 M. S. Ladinsky, J. M. Pierson and J. R. McIntosh, *J. Microsc. (Oxford, UK)*, 2006, **224**, 129–134.
16 L. F. Gladden, M. D. Mantle and A. J. Sederman, *Adv. Catal.*, 2006, **50**, 1–75.
17 L. F. Gladden, *Top. Catal.*, 2003, **24**, 19–28.
18 J. Radon, *Ber. Verh. K. Saechs. Ges. Wiss. Leipzig Math.-Phys. Kl.*, 1917, **69**, 262–265.
19 S. R. Deans, *The Radon transform and some of its applications*, Wiley, New York, Chichester, 1983.
20 G. N. Ramachandran and A. V. Lakshminarayanan, *Proc. Natl. Acad. Sci. U. S. A.*, 1971, **68**, 2236–2240.
21 W. Hoppe, R. Langer, G. Knesch and C. Poppe, *Naturwissenschaften*, 1968, **55**, 333–336.
22 R. A. Crowther, D. J. de Rosier and A. Klug, *Proc. R. Soc. London, Ser. A*, 1970, **317**, 319.
23 M. Radermacher, in *Electron tomography : three-dimensional imaging with the transmission electron microscope*, ed. J. Frank, Plenum Press, New York/London, 1992, pp. 91–116.
24 G. T. Herman, *Image Reconstruction From Projections, The Fundamentals of Computerised Tomography*, Academic Press, New York, 1980.
25 P. F. C. Gilbert, *Proc. R. Soc. Lond., Ser. B.*, 1972, **182**, 89.
26 The fidelity of a reconstruction can be improved further by noting that each recorded image is a 'perfect' reference projection. If an (imperfect) reconstruction is re-projected back along the original projection direction, the re-projections, in general, will not be identical to the original images. The difference, characteristic of the deficiency of the reconstruction, can be backprojected to generate a 'difference' reconstruction, which can be used to correct the original reconstruction, to constrain the reconstruction to agree better with the original set of images. A single operation

will not fully correct the reconstruction and the comparison must be repeated iteratively until a 'best' solution is reached. For more details see ref. 27–31.

27 R. A. Crowther and A. Klug, *J. Theor. Biol.*, 1971, **32**, 199.
28 S. H. Bellman, R. Bender, R. Gordon and J. E. Rowe, *J. Theor. Biol.*, 1971, **32**, 205.
29 I. M. Sezan, *Ultramicroscopy*, 1992, **40**, 55–67.
30 R. W. Gerchberg and W. O. Saxton, *Optik*, 1971, **34**, 275.
31 J. Frank, *Three-Dimensional Electron Microscopy of Macromolecular Assemblies*, Academic Press, San Diego, 1996.
32 V. E. Cosslett and W. C. Nixon, *X-Ray Microscopy*, Cambridge University Press, London, 1960.
33 D. Attwood, *Soft X-Rays and Extreme Ultraviolet Radiation: Principles and Applications*, Cambridge University Press, London, 2000.
34 E. Di Fabrizio, F. Romanato, M. Gentili, S. Cabrini, B. Kaulich, J. Susini and R. Barrett, *Nature*, 1999, **401**, 895–898.
35 W. Yun, B. Lai, A. A. Krasnoperova, E. Di Fabrizio, Z. Cai, F. Cerrina, Z. Chen, M. Gentili and E. Gluskin, *Rev. Sci. Instrum.*, 1999, **70**, 3537–3541.
36 W. L. Chao, B. D. Hartneck, J. A. Liddle, E. H. Anderson and D. T. Attwood, *Nature*, 2005, **435**, 1210–1213.
37 G.-C. Yin, M.-T. Tang, Y.-F. Song, F.-R. Chen, K. S. Liang, C.-H. Ko and H.-P. D. Shieh, *Appl. Phys. Lett.*, 2006, **88**, 241115.
38 D. Attwood, *Nature*, 2006, **442**, 642–643.
39 M. A. Le Gros, G. McDermott and C. A. Larabell, *Curr. Opin. Struct. Biol.*, 2005, **15**, 593–600.
40 C. G. Schroer, M. Kuhlmann, T. F. Gunzler, B. Lengeler, M. Richwin, B. Griesebock, D. Lutzenkirchen-Hecht, R. Frahm, E. Ziegler, A. Mashayekhi, D. R. Haeffner, J. D. Grunwaldt and A. Baiker, *Appl. Phys. Lett.*, 2003, **82**(19), 3360–3362.
41 A. C. Kak and M. Slaney, *Principles of Computerized Tomographic Imaging*, 1988, IEEE, New York.
42 D. Sayre, in *Imaging Processes and Coherence in Physics. Springer Lecture Notes in Physics*, ed. M. Schlenker, M. Fink, J. P. Goedgebuer, C. Malgrange, J. Ch. Viénot and R. H. Wade, Springer, Berlin, 1980, **112**, 229–235.
43 J. Miao, P. Charalambous, J. Kirz and D. Sayre, *Nature*, 1999, **400**, 342–344.
44 S. Marchesini, H. He, H. N. Chapman, S. P. Hau-Riege, A. Noy, M. R. Howells, U. Weierstall and J. C. H. Spence, *Phys. Rev. B: Condens. Matter Mater. Phys.*, 2003, **68**, 140101.
45 H. N. Chapman, A. Barty, S. Marchesini, A. Noy, S. P. Hau-Riege, C. Cui, M. R. Howells, R. Rosen, H. He, J. C. H. Spence, U. Weierstall, T. Beetz, C. Jacobsen and D. Saphiro, *J. Opt. Soc. Am. A*, 2006, **23**, 1179–1200.
46 With the recent advent of aberration-corrected electron microscopes (see for example ref. 47) even greater precision and resolution may be achievable.
47 M. Watanabe, D. W. Ackland, C. J. Kiely, D. B. Williams, M. Kanno, R. Hynes and H. Sawada, *JEOL News*, 2006, **41**, 2–7.
48 J. M. Thomas, P. A. Midgley, T. J. V. Yates, J. S. Barnard, R. Raja, I. Arslan and M. Weyland, *Angew. Chem., Int. Ed.*, 2004, **43**, 6745–6747.
49 P. B. Hirsch, A. Howie, R. B. Nicholson, D. W. Pashley and M. J. Whelan, *Electron Microscopy of Thin Crystals*, Krieger, New York, 1977.
50 D. B. Williams and C. B. Carter, *Transmission Electron Microscopy*, Plenum Press, New York, 1996.
51 D. J. de Rosier and A. Klug, *Nature*, 1968, **217**, 130–134.
52 R. G. Hart, *Science*, 1968, **159**, 1464–1467.
53 P. W. Hawkes, in *Electron tomography: three-dimensional imaging with the transmission electron microscope*, ed. J. Frank, Plenum Press, New York; London, 1992, 17.
54 R. J. Spontak, M. C. Williams and D. A. Agard, *Polymer*, 1988, **29**(3), 387–395.
55 O. Medalia, I. Weber, A. S. Frangakis, D. Nicastro, G. Gerish and W. Baumeister, *Science*, 2002, **298**, 1209–1213.
56 J. J. Fernandez, S. Li and R. A. Crowther, *Ultramicroscopy*, 2006, **106**, 587–596.
57 R. F. Egerton, *J. Electron Microsc.*, 1999, **48**(6), 711–716.
58 M. Koguchi, H. Kakibayashi, R. Tsuneta, M. Yamaoka, T. Niino, N. Tanaka, K. Kase and M. Iwaki, *J. Electron Microsc.*, 2001, **50**(3), 235–241.
59 A. J. Koster, A. Van Den Bos and K. D. Van Der Mast, *Ultramicroscopy*, 1987, **21**, 209–221.
60 M. C. Lawrence, in *Electron tomography: three-dimensional imaging with the transmission electron microscope*, ed. J. Frank, Plenum Press, New York; London, 1992, 197.
61 P. A. Midgley and M. Weyland, *Ultramicroscopy*, 2003, **96**, 413–431.
62 I. Arslan, J. R. Tong and P. A. Midgley, *Ultramicroscopy*, 2006, **106**, 994–1000.
63 J. Tong, I. Arslan and P. A. Midgley, *J. Struct. Biol.*, 2006, **153**(1), 55–63.
64 M. Radermacher and W. Hoppe, *Proceedings of the 7th European Congr. Electron Microscopy*, Den Haag, The Netherlands, ed. P. Brederoo and W. De Priester, 7th European Congr. Electron Microscopy Foundation, Leiden, The Netherlands, 1980, **1**, 132–133.
65 A. P. Leis, M. Beck, M. Gruska, C. Best, R. Hegerl, W. Baumeister and J. W. Leis, *IEEE Signal Processing Magazine*, 2006, 95–103.
66 B. J. Marsh, D. N. Mastronade, K. F. Buttle, K. E. Howell and J. R. McIntosh, *Proc. Natl. Acad. Sci. U. S. A.*, 2001, **98**, 2399–2406.
67 W. Baumeister, *Curr. Opin. Struct. Biol.*, 2002, **12**, 679.
68 O. Medalia, I. Weber, A. S. Frangakis, D. Nicastro, G. Gerish and W. Baumeister, *Science*, 2002, **298**, 1209–1213.
69 M. Beck, F. Förster, M. Ecke, J. M. Plitzko, F. Melchior, G. Gerish, W. Baumeister and O. Medalia, *Science*, 2004, **306**, 1387–1390.
70 A. Sheffel, M. Gruska, D. Faivre, A. Linaroudis, J. M. PlitzKo and D. Schüler, *Nature*, 2006, **440**, 110–114.
71 A. Komeili, Z. Liu, D. K. Newman and G. J. Jensen, *Science*, 2006(311), 242–245.
72 F. S. Bates and G. H. Fredrickson, *Annu. Rev. Phys. Chem.*, 1990, **41**, 525–557.
73 H. Jinnai, H. Hasegawa, Y. Nishikawa, G. J. A. Sevink, M. B. Braunfeld, D. A. Agard and R. J. Spontak, *Macromol. Rapid Commun.*, 2006, **27**, 1424–1429.
74 In weak-beam dark-field (WBDF) imaging, off-axis illumination is employed to encode detailed information on local lattice displacement into the diffracted beam. Under WBDF conditions, diffraction contrast yields an image of a dislocation that is narrow in width, and close to the dislocation core.
75 J. S. Barnard, J. Sharp, J. R. Tong and P. A. Midgley, *Science*, 2006, **313**, 319.
76 J. S. Barnard, J. Sharp, J. R. Tong and P. A. Midgley, *Philos. Mag.*, 2006, **86**, 4901–4922.
77 A. C. Twitchett, R. E. Dunin-Borkowski, T. J. V. Yates, P. A. Midgley and S. B. Newcomb, *J. Phys. Conf. Ser.*, 2006, **26**, 29–32.
78 S. J. Pennycook, *Ultramicroscopy*, 1989, **30**, 58–69.
79 K. Inoke, K. Kaneko, M. Weyland, P. A. Midgley, K. Higashida and Z. Horita, *Acta Mater.*, 2006, **54**, 2957–2963.
80 D. A. Muller, B. Edwards, E. J. Kirkland and J. Silcox, *Ultramicroscopy*, 2001, **86**, 371–380.
81 A. Howie, *J. Microsc.*, 1979, **177**, 11–23.
82 P. B. Hirsch, A. Howie, R. B. Nicholson, D. W. Pashley and M. J. Whelan, in *Electron Microscopy of Thin Crystals*, Krieger, New York, 2nd edn, 1977.
83 S. J. Pennycook and P. D. Nellist, in *Impact of Electron and Scanning Probe Microscopy on Materials Research*, ed. D. G. Rickerby, Kluwer, 1999, 161.
84 P. A. Midgley, M. Weyland, J. M. Thomas and B. F. G. Johnson, *Chem. Commun.*, 2001, **18**, 907–908.
85 M. Weyland, P. A. Midgley and J. M. Thomas, *J. Phys. Chem. B*, 2001, **105**(33), 7882–7886.
86 R. E. Dunin-Borkowski, S. B. Newcomb, T. Kasami, M. R. McCartney, M. Weyland and P. A. Midgley, *Ultramicroscopy*, 2005, **103**, 67–81.
87 A. J. Koster, U. Ziese, A. J. Verklej, A. H. Hansen and K. P. de Jong, *J. Phys. Chem. B*, 2002, **106**, 11905–11909.
88 A. H. Hansen, A. J. Koster and K. P. de Jong, *J. Phys. Chem. B*, 2000, **104**, 9368–9370.
89 K. P. de Jong and A. J. Koster, *ChemPhysChem*, 2002, **3**, 776–780.

90 U. Ziese, K. P. de Jong and A. J. Koster, *Appl. Catal., A*, 2004, **260**, 71–74.

91 F. Schüth, K. S. W. Sing and J. Weitkamp, in *Handbook of Porous Materials*, Wiley-VCH,Weinheim, 2002.

92 J. M. Thomas, B. F. G. Johnson, R. Raja, G. Sankar and P. A. Midgley, *Acc. Chem. Res.*, 2003, **36**(1), 20–30.

93 J. M. Thomas and R. Raja, *Annu. Rev. Mater. Res.*, 2005, **35**, 315–320.

94 P. A. Midgley, J. M. Thomas, L. Laffont, M. Weyland, R. Raja, B. F. G. Johnson and T. Khimyak, *J. Phys. Chem. B*, 2004, **108**, 4590–4592.

95 J. M. Thomas and P. A. Midgley, *Chem. Commun.*, 2004, **11**, 1253–1267.

96 E. P. W. Ward, I. Arslan, P. A. Midgley, A. Bleloch and J. M. Thomas, *Chem. Commun.*, 2005, **46**, 5805–5807.

97 A. B. Hungría, R. Raja, R. D. Adams, B. Captain, J. M. Thomas, P. A. Midley, V. Golovko and B. F. G. Johnson, *Angew. Chem., Int. Ed.*, 2006, **45**, 4782–4785.

98 R. Raja, T. Khimyak, J. M. Thomas, S. Hermans and B. F. G. Johnson, *Angew. Chem., Int. Ed.*, 2001, **40**(24), 4638–4642.

99 S. Hermans, R. Raja, J. M. Thomas, B. F. G. Johnson, G. Sankar and D. Greeson, *Angew. Chem., Int. Ed.*, 2006, **40**(7), 1211–1215.

100 A. B. Hungria, N. D. Browning, R. P. Erni, M. Fernandez-Garcia, J. C. Conesa, J. A. Perez-Omil and A. Martinez-Arias, *J. Catal.*, 2005, **235**(2), 251–261.

101 S. Mejía-Rosales, C. Fernández-Navarro, E. Pérez-Tijerina, J. M. Montejano-Carrizales and M. José-Yacamán, *J. Phys. Chem. B*, 2006, **110**, 12884–12889.

102 J. M. Thomas, *Ultramicroscopy*, 1982, **8**, 13.

103 P. A. Midgley, M. Weyland, T. J. V. Yates, I. Arslan, R. E. Dunin-Borkowski and J. M. Thomas, *J. Microsc.*, 2006, **223**(3), 185–190.

104 A. Tonomura, *Electron Holography*, Springer, Berlin, 1999.

105 D. S. McKay, E. K. Gibson, Jr., K. L. Thomas-Keprta, H. Vali, C. S. Romanek, S. J. Clemett, X. D. F. Chillier, C. R. Maechling and R. N. Zare, *Science*, 1996, **273**, 924–930.

106 W. Zhou, J. M. Thomas, D. S. Shephard, B. F. G. Johnson, T. Maschmeyer, D. Ozkaya, R. G. Bell and Q. Ge, *Science, 1998*, 5364, **280**, 705–708.

107 Y. Sakamoto, T.-W. Kim, R. Ryoo and O. Terasaki, *Angew. Chem., Int. Ed.*, 2004, **43**(39), 5231–5234.

108 T. J. V. Yates, J. M. Thomas, J.-J. Fernandez, O. Terasaki, R. Ryoo and P. A. Midgley, *Chem. Phys. Lett.*, 2006, **418**(4–6), 540–543.

109 G. Mobus and B. J. Inkson, *Appl. Phys. Lett.*, 2001, **79**(9), 1369–1371.

110 M. Weyland and P. A. Midgley, *Microsc. Microanal.*, 2003, **9**(6), 542–555.

111 R. F. Egerton, in *Electron Energy Loss Spectroscopy in the Electron Microscope*, Plenum Press, New York, 2nd edn, 1996.

112 F. Hofer, W. Grogger, G. Kothleitne and P. Warbichler, *Ultramicroscopy*, 1997, **67**(1–4), 83–103.

113 P. J. Thomas and P. A. Midgley, *Ultramicroscopy*, 2001, **88**, 179–186.

114 P. J. Thomas and P. A. Midgley, *Ultramicroscopy*, 2001, **88**, 187–194.

115 M. H. Gass, K. K. Koziol, A. H. Windle and P. A. Midgley, *Nano Lett.*, 2006, **6**(3), 376–379.

116 R. D. Leapman, C. E. Fiori, K. E. Gorlen, C. C. Gibson and C. R. Swyt, *Ultramicroscopy*, 2004, **100**(1–2), 115–125.

117 M. Weyland, T. J. V. Yates, R. E. Dunin-Borkowski, L. Laffont and P. A. Midgley, *Scr. Mater.*, 2006, **55**, 29–33.

118 N. Browning (personal communication).

119 J. M. Thomas and P. L. Gai, *Adv. Catal.*, 2004, **48**, 171–227.